Supplement of Atmos. Meas. Tech., 19, 3625–3665, 2026
https://doi.org/10.5194/amt-19-3625-2026-supplement

Atmospheric Measurement Techniques
Open Access
EGU

Supplement of

From real-time to long-term source apportionment of PM_{10} using high-time-resolution measurements of aerosol physical properties: methodology and example application at an urban background site (Aosta, Italy)

Henri Diémoz et al.

Correspondence to: Henri Diémoz (h.diemoz@arpa.vda.it)

S1 Map of Aosta

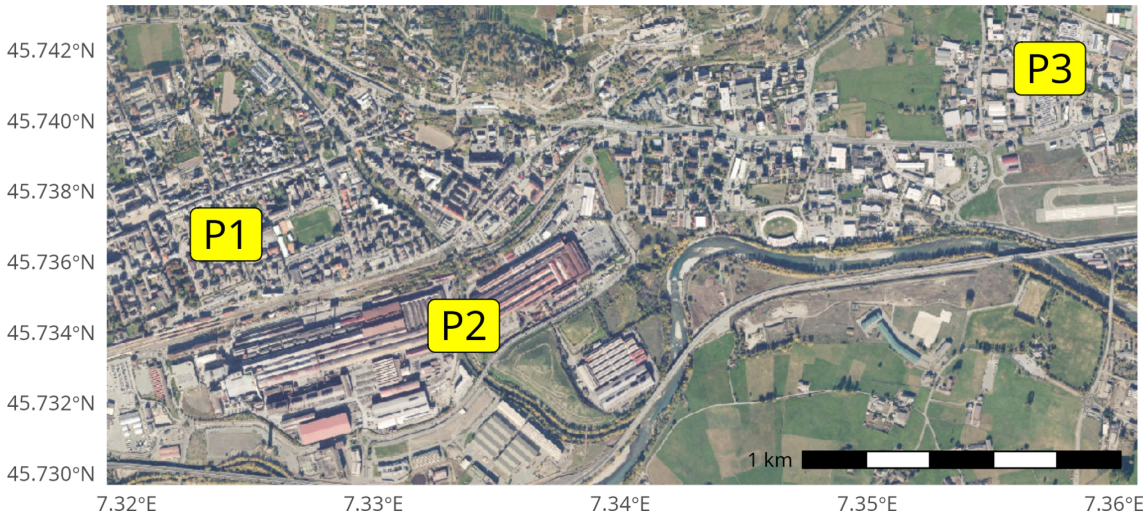

Figure S1: Aerial photograph of Aosta city taken in 2021 (Regione Valle d'Aosta, 2021), with labels indicating key locations: the Aosta–downtown air quality station (P1), the steel mill (P2), and the Aosta–Saint-Christophe solar-atmospheric observatory (P3).

S2 Supplementary details on Palas Fidas 200

The Palas Fidas 200, currently housed in a temperature-stabilised air quality cabin at the Aosta–Downtown station, was originally acquired as the 200S variant, which features a stainless-steel weather-proof casing for outdoor operation. Ambient air is sampled at a rate of 4.8 L min^{-1} into the instrument, with condensation effects mitigated by the integrated 'Intelligent Aerosol Drying System' (IADS). This module dynamically adjusts the sample temperature based on ambient conditions (measured by an integrated weather station), at a minimum temperature of 23°C. The maximum heating output is 90 W. Without temperature regulation, water condensating on particles in high humidity conditions could cause distorting size measurements. Additionally, according to the manual (PALAS GmbH, 2016), residual water content is detected, and the mass of liquid droplets is subtracted to improve accuracy.

Particle detection is based on the scattering of light from a broadband source (LED) at a 90° angle (Pletscher et al., 2016). Border zone errors are removed using a specialized T-aperture optical design, and coincidence events are corrected through digital particle analysis. The instrument processes particle size distributions and retrieves PM concentrations using its built-in proprietary algorithm, `PM_ENVIRO_0011`. For completeness, the operational steps of this algorithm, only briefly outlined in the manual (PALAS GmbH, 2016), are reported below:

1. The initial particle size distribution, referred to a latex-equivalent diameter, is adjusted to a distribution with a representative refractive index for the environment. It is presumable that this step is introduced to mitigate the sensitivity of OPCs measurements to refractive index (Ferrero et al., 2011; Chien et al., 2016), though some studies suggest these errors are minimal in urban settings (Hasheminassab et al., 2014; Sowlat et al., 2016).

2. Optical diameters are converted to aerodynamic diameters (the manual provides no further details on the method used).

3. The shape of the particle size distribution is analysed, and density parameters are derived.

4. Particle mass concentration is estimated using these size-dependent conversion functions.

Verification of equivalence (e.g., Marsteen and Hak, 2021) has been routinely performed at the Aosta–Downtown against the gravimetric method. The Palas Fidas 200 consistently demonstrated relative observation uncertainties within 25 % at the PM_{10} EU daily limit value, in agreement with Directive

2008/50/EC (European Commission, 2008). Hence, no corrections to the Fidas PM_{10} concentrations were deemed necessary. Monthly maintenance includes the following procedures: automatic offset adjustment, leakage testing, sampling head cleaning, pump filter replacement, sampling flow rate measurement, photomultiplier tube (PMT) testing using monodust aerosols, and pump suction output verification with replacement if efficiency drops below 80 %.

We set the sampling resolution of the Fidas to 1 min instead of the default 1 s. This adjustment is particularly important because we found that coarse (and sparser) particles are not adequately sampled at higher frequencies. Particle size distribution and PM concentration datasets are automatically extracted from the instrument via the Fidas MODBUS interface, eliminating the need for manual operation of the 'PDAnalyze' program.

S2.1 Fidas Palas 200 measurement uncertainty

A comprehensive and instrument-specific assessment of the measurement uncertainty of the optical particle counter (OPC) employed here is beyond the scope of the present work, and full laboratory characterisation of the Fidas system was not feasible within this study. Additionally, such an assessment is inherently challenging for this instrument, as the detected signals are processed dynamically by proprietary algorithms in which particle properties are treated as variable quantities, and intermediate processing steps are not accessible to the user. From a practical standpoint, this limits the possibility of rigorously quantifying the 'sizing precision' through controlled experiments using synthetic aerosols. It should also be emphasised that the Fidas retrieval algorithm was originally conceived with the aim not to provide an absolute 'true' particle size distribution (PSD), but rather to derive particulate matter (PM) concentrations equivalent to the reference gravimetric method. In this respect, the instrument has been demonstrated to yield PM values with comparatively low uncertainty.

For these reasons, only a simplified and conceptual discussion is reported here. Several sources of uncertainty can be identified:

- **Counting statistics**. In the present study, PSD data are measured over a time interval of 1 min and averaged over 1 h. The effective analysed air volume during 1 h (i.e. the volume illuminated by the optical beam and effectively probed, which differs from the total flow rate) is approximately $V_{\text{eff}} \sim 9.2 \times 10^3$ cm^3 (S. Hogekamp, Palas GmbH, personal communication). An estimate of the number of particles detected in each size bin can be obtained by multiplying the median particle number size distribution reported by the instrument by V_{eff} and by $\log_{10}(D_p)$. This yields particle counts ranging from approximately 10^5 for the smallest diameter bins ($D_p \sim 0.18$ μm) to about 10 particles at $D_p \sim 10$ μm. Assuming Poisson counting statistics, the corresponding relative uncertainty is given by

  $$\frac{\sigma_N}{N} = \frac{1}{\sqrt{N}}, \tag{S1}$$

  leading to values in the range 0.16 % to 30 %. It should be considered that ambient PM_{10} concentrations in Aosta are generally low, and notably large particles are relatively rare. Hence, median conditions as those selected above are not the most relevant circumstances for the application of the RASPBERRY methodology. Considering higher percentiles of the particle number distribution (e.g. 80th–90th percentile) instead of the median leads to increased particle counts and therefore reduced relative uncertainties, of the order of 0.1 % for the smallest particles and 15 % for the largest ones. Notably, the latter is of the same order of magnitude as the uncertainty adopted in the PMF analysis (Sect. S7).

  It is important to stress that this source of uncertainty arises purely from counting statistics and is therefore common to all particle-counting instruments. In the present estimate, the only instrument-specific parameter is the effective probed volume.

- **Sensor and sizing uncertainty**. Without going into further detail, it is reasonable to assume that the repeatability of particle sizing for identical, monodisperse particles is on the order of a few percent for the instrument considered here (S. Hogekamp, Palas GmbH, personal communication). This contribution reflects the intrinsic variability of the optical detection and sizing process.

– **Multi-channel and modal analysis**. The identification and quantification of PMF factors in the particle size distribution and their PM contributions, as performed in this work, relies on measurements across multiple adjacent size channels. This inherently reduces the impact of the random component of the uncertainty associated with individual bins. The EVLS method employed here (Sect. S9) explicitly propagates both measurement uncertainty and profile uncertainty into the estimation of factor contribution uncertainties, thereby accounting for these effects in a consistent manner.

Finally, it should be emphasised that the uncertainty values used as input to the PMF analysis are not limited to measurement uncertainties alone. Rather, they are derived through a broader procedure that also accounts for the coexistence of different physical quantities within the source apportionment framework, as well as model-related considerations (Sect. S7).

S3 Choice of aethalometer wavelengths to calculate the Delta-C quantity

Various wavelength combinations can be employed to calculate Delta-C, for example 370 nm or 470 nm can be chosen as the lower limit, and 880 nm or 950 nm as the upper limit.

For our dataset, the choice of the upper limit is unimportant, as also found by Zotter et al. (2017), since the correlation index between the combinations using 880 nm and 950 nm is nearly 1 (0.99988). Hence, we use 880 nm, the conventional wavelength for defining eBC. As for the lower limit, our choice is based on two factors. First, previous investigations in Aosta and its outskirts (Diémoz et al., 2020) found that the correlation index between levoglucosan concentrations, an unambiguous marker of fresh biomass burning, and aethalometer measurements at 370 nm is very high (ranging from 0.82 to 0.92, depending on the site). Second, we analysed the patterns of the difference between aethalometer mass concentrations at 370 nm and 880 nm, as well as between 470 nm and 880 nm, at different temporal scales (Fig. S2). The results indicate that the former quantity exhibits greater variability between night and day, and between winter and summer, suggesting that it may more closely track the variations in the biomass burning contribution to PM than the latter quantity.

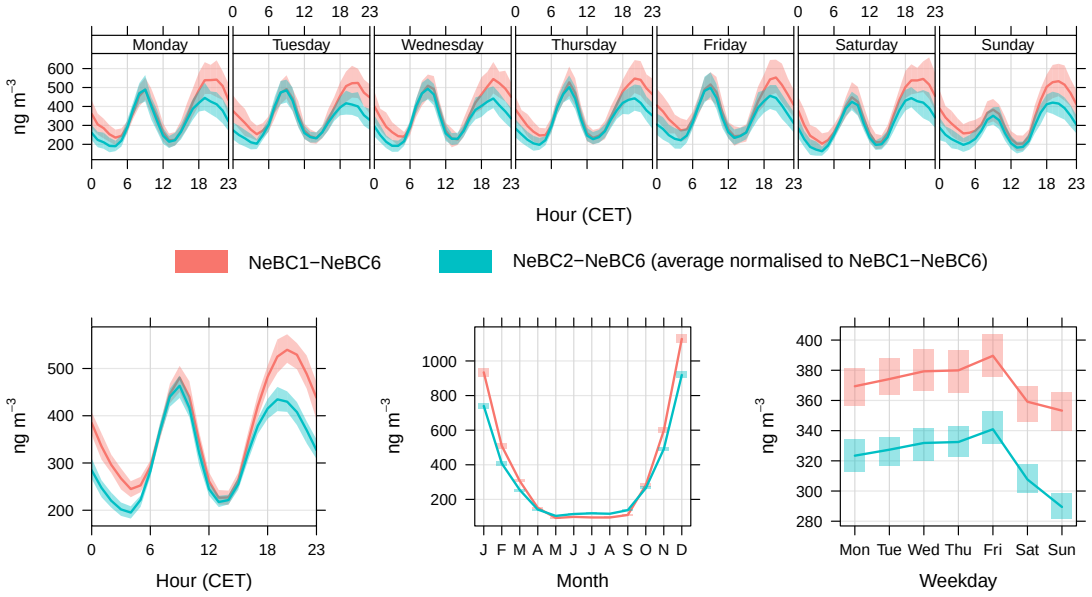

Figure S2: Average time patterns of the difference between $\mathrm{NeBC}_{370\ \mathrm{nm}}$ (NeBC1) and $\mathrm{NeBC}_{880\ \mathrm{nm}}$ (NeBC6), as well as between $\mathrm{NeBC}_{470\ \mathrm{nm}}$ (NeBC2) and $\mathrm{NeBC}_{880\ \mathrm{nm}}$, at different temporal scales. For ease of visualisation, the latter quantity has been normalised, on average, to the former.

It should be noted that the influence of volatile or secondary biogenic organic compounds at

370 nm (Vecchi et al., 2014; Romonosky et al., 2016; Xie et al., 2019) is sometimes considered an interfering factor in determining the biomass burning contribution (Zotter et al., 2017). However, if such interference were significant at our site, the source apportionment algorithm should have identified it as a separate factor. Nonetheless, the strong agreement between the biomass burning contribution derived from RASPBERRY and that obtained from the chemical PMF (correlation index $\rho = 0.95$, Fig. 8 in the main text) retrospectively validates this specific choice of wavelengths. Therefore, in this study, we retain the original definition of Delta-C by Allen et al. (2011) and Wang et al. (2011) using the two-wavelength aethalometer, i.e.:

$$\text{Delta-C} = \text{NeBC}(370\text{ nm}) - \text{NeBC}(880\text{ nm}) \tag{S2}$$

S4 Supplementary details on Aerosol Magee Scientific AE33 aethalometer

Two primary instrumental artefacts influence the accuracy of aethalometer measurements and require correction: the filter-loading effect and the multiple-scattering enhancement effect (Weingartner et al., 2003). The AE33 dual-spot technology compensates for the filter-loading effect in real time, while the multiple-scattering enhancement is addressed using a scattering correction coefficient (C). In this study, we employ the default instrument manufacturer fixed parameters (C_0= 1.39 for filter tape M8060; nominal MAC value of 7.77 $m^2\,g^{-1}$ at 880 nm) and, accordingly, we adopt the term NeBC ('nominal' eBC, Savadkoohi et al., 2024) to denote the AE33 output obtained under nominal settings. Although recent research demonstrates that using instrument- and site-specific parameters (Grange et al., 2020; Ferrero et al., 2024), or harmonised coefficients (Zanatta et al., 2016; Savadkoohi et al., 2024), leads to more accurate determination of the absorption coefficients, our approach is guided by two criteria: (i) ensuring the algorithm is simple and straightforward to implement, and (ii) assuming that temporal and spectral variations in aerosol light absorption are more important in PMF analysis than the absolute accuracy of b_{abs} values. Moreover, determining site-specific parameters such as the MAC requires data from ancillary sources, which might not be available at all locations. While these refinements are essential for analysing long-term trends (Grange et al., 2020; Savadkoohi et al., 2024), they are left for future research. However, we note that the correlation, in Aosta–Downtown, between EC from chemical analyses and NeBC at both 880 and 950 nm is already very strong (Pearson's $\rho = 0.93$).

The following data quality controls are applied on the aethalometer measurements:

- Occasional negative values at the 1-minute scale are retained to avoid biases in average calculations. However, negative NeBC values in 1-hour averages are excluded.
- Measurements yielding negative Delta-C at the 1-hour scale are also removed.
- Extremely high NeBC concentrations (>15 000 ng m^{-3}) are discarded, as these outliers are often associated with circumstantial events or measurement anomalies unsuitable for algorithm training.
- Quality control thresholds proposed by Aujay-Plouzeau (2020), including AAE and the R^2 of spectral fits at the 15-minute scale, were tested but not adopted since, in our case, they were not always representative of measurement quality.
- The final dataset was visually inspected to remove any remaining anomalous data.

Regular maintenance is performed monthly and includes: clean air test; inspection and cleaning of the optical chamber, insect trap, and sampling line; lubrication of the optical chamber cursors; ND filter test; bypass cartridge replacement if necessary; stability test.

An important aspect of our AE33 setup relates to its sampling line. During a 2019 experimental campaign with a mobile laboratory (Diémoz et al., 2020), the AE33 was operated without a sampling head for technical reasons. This configuration was inadvertently replicated in the permanent installation at the Aosta–Downtown station, resulting in BC measurements in total suspended particles (TSP). This oversight was identified recently and an update to the setup with a PM_{10} cyclone and a drier is scheduled. Future studies will assess the impact of this change, however it is uncertain whether

the absence of a PM_{10} inlet has significantly influenced measurements. Indeed, the majority of light-absorbing particles reside in the fine fraction. Some high-frequency noise is observed in 1-minute NeBC data at very low concentrations, such as during summer, potentially amplified by the lack of a drier. To mitigate these effects, aethalometer measurements were averaged to 1-hour intervals, and data from all instruments in Aosta–Downtown were harmonised to this temporal resolution. This averaging period was considered appropriate to focus on PM_{10} sources influencing the urban background on representative temporal and spatial scales, while also ensuring robust statistics over the multi-year dataset analysed in this study. Nevertheless, the RASPBERRY algorithm can in principle be applied to data at higher temporal resolution when appropriate measurements and signal-to-noise conditions are available.

S5 On the inclusion of gases in the physical PMF

Recent guidelines of the European project RI-URBANS (Petit et al., 2024) suggest including NO_x in PMF analyses. This practice may be useful for supporting the factor-source attribution based on the factor NO_x is associated with. In such cases, NO_x should be introduced into the PMF as weak species (e.g., Vörösmarty et al., 2024) in order to prevent them from exerting an excessive influence on the separation of the factors (see below).

However, it should be considered that in Alpine environments, particularly during winter, NO_x does not exclusively trace traffic emissions but also biomass combustion, and that Aosta is a relatively small, low-traffic city (33,000 inhabitants; Diémoz et al., 2019, 2020, 2021). In the chemical PMF, for example, the correlation of NO, NO_2, and NO_x with the biomass-burning factor is higher ($R^2 = 0.63$, 0.63, and 0.67, respectively) than with the traffic factor ($R^2 = 0.56$, 0.45, and 0.53).

For this reason, we were cautious about using NO_x as a strong species contributing to the separation of the factors. Several tests performed during the development of this work indicate that, when NO_x is introduced as a strong species, the agreement between the chemical and physical PMF deteriorates and, in some cases, the physical PMF yields unrealistic solutions. For example:

- When NO_x is introduced with an uncertainty of 5–10 %, the seasonal cycle of NO_x is poorly reproduced by the PMF, with NO being strongly underestimated during winter.
- When the uncertainty assigned to NO_x is reduced, both NO and NO_2 are forced to be reproduced more accurately. However, the reconstruction of DeltaC deteriorates ($Q/Q_{exp} = 20$), and the contributions of PM_{bb} and PM_{ff} decrease by approximately a factor of three (i.e., to ∼3 %). In some configurations, an additional NO-rich factor separates from the factor associated with traffic emissions.

This behaviour is likely related to the fact that the relationship between NO_x and aerosol, as also discussed by Rivas et al. (2020), depends on several factors: (a) meteorology and atmospheric dynamics (e.g. solar radiation availability, temperature, etc.); (b) long-term changes in the vehicle fleet; and (c) driving conditions. Consequently, the ratio between NO_x and traffic-related PM can vary throughout the day, between seasons, and over longer time scales as the ones addressed here. In addition, if as we expect the exhaust fraction is not fully captured by the OPC and the PMF is forced to maintain a strong correlation with NO_x, the model may compensate this constraint by reducing the PM_{10} mass attributed to traffic.

S6 Chemical PMF configuration

As outlined in Sect. 2.4 of the main text, two separate chemical PMF analyses are performed due to the alternating sampling schedule and differing chemical characterisations. No missing values are included in both PMF input datasets, and new year's days are excluded from the analysis each year. Dataset 1 (water-soluble ions alongside EC/OC and levoglucosan) consists of 383 samples and 12 variables. Ca^{2+} and Mg^{2+} are set as weak, given their high proportion of values at or near detection limits, 23 % and 21 % respectively. This choice may slightly affect the PMF output, particularly the separation of traffic-related and coarse particle resuspension contributions. $NH4^{+}$ is also classified as weak as recent findings suggest that ammonium volatilisation likely occurred post-sampling due to

operational practices with the sequential sampler and filter storage. Updated procedures have since been introduced to address these issues. PM_{10} is set as the total variable, while the remaining eight variables are classified as strong. Dataset 2 (water-soluble ions and metals) includes 699 samples and 18 species. The following species are treated as weak: Al, as it tends to form an isolated factor, a fact that is only partially correlated with long-range transport of desert dust (contamination of samples or local sources other than desert dust are possible reasons); Zn, due to a spurious concentration increase over time likely caused by analytical issues; Co, since many measurements are close to detection limits, which varies over time with changes in analytical techniques; NH_4^+, Ca^{2+}, and Mg^{2+}, for the same reasons outlined for the first dataset. Additionally, days with single outlier values for Cd, Cu, Zn, Co, Pb, and Mg are excluded from the analysis.

S7 Physical PMF uncertainty configuration

The uncertainty framework employed in this study follows the methodology outlined by Vörösmarty et al. (2024), in which the PMF input uncertainty is parametrised as in Eqs. (4) and (5) of the main text. This formulation essentially represents a semi-empirical error model, with notation likely inherited from earlier PMF implementations (PMF2), and separates the uncertainty into two components representing common sources of uncertainty in aerosol measurements: (i) baseline instrument/analysis noise, ensuring a minimum uncertainty even when concentrations are small; and (ii) a concentration-dependent error, which increases proportionally with the measured concentration. The interested reader is referred to that work, and the references therein, for further details. Here we instead present an objective and reproducible workflow describing, step by step, how the free coefficients A, α, and C_3 were selected:

1. Choice for A and α started from relevant ranges suggested in the aforementioned study and in the scientific literature (e.g., Zhou et al., 2005a; Ogulei et al., 2006, 2007; Gu et al., 2011), i.e. 0.01 to 0.05 for the product $A \times \alpha$. In our case, $A = 1$ was assigned to size channels and optical absorption, and $\alpha = 0.01$ was used as an initial value, following Vörösmarty et al. (2024).

2. Choice for C_3 started from values between 0.01 and 0.5. For example, Vörösmarty et al. (2024) select 0.10 for most of their channels. A value of about 10 % represents a reasonable *a priori* estimate of the uncertainty when no additional information is available, therefore C_3 was initially set to this value in our case.

3. We then ensured that the total variable (e.g., PM_{10}) did not influence the factorisation by setting it as 'weak' in the PMF (or by assigning $A = 3$ and $C_3' = C_3 \times 3$).

4. An initial PMF run was performed, and the residual distribution (Q/Q_{exp}) for each 'species' (VSD channels from OPC and aethalometer spectral absorption at the measured wavelengths) was recorded. At this stage, the volume distribution component typically dominated the profile splitting and was better reproduced by the PMF, with the exception of the largest size ranges (as also reported by Vörösmarty et al., 2024), whereas spectral absorption contributed only marginally to the separation and was not well reproduced (resulting in a high Q/Q_{exp} ratio). This behaviour arises from the larger number of 'channels' associated with particle size (OPC measurements) compared with those related to multispectral optical absorption (aethalometer).

5. We gradually adjusted the uncertainty until three criteria were simultaneously satisfied: (i) the factor contributions remained as uncorrelated as possible; (ii) the scaled residuals fell within the expected range (± 3, Norris et al., 2014); and (iii) the resulting profiles and contributions were physically plausible.

6. In our case, reducing the residuals (and the Q/Q_{exp} ratio) for the largest size channels without artificially splitting the coarse 'local resuspension' factor into two modes required increasing their uncertainty. This resulted in $C_3 = 0.3$ for size channels with particles larger than 2 ţm and $C_3 = 0.4$ for particles above 6 ţm. The 2 ţm and 6 ţm thresholds were selected as representative of the desert dust and coarse resuspension modes, based on previous literature (see main text) and the examination of the temporal evolution of the volume size distributions. Indeed, these C_3 values improved the separation between desert dust and local resuspension contributions. Larger

uncertainty values tended to merge these contributions, whereas smaller values tended to split the local resuspension factor into multiple modes.

7. Conversely, in order for the absorption measurements to contribute effectively to shaping the factor profiles, their uncertainty had to be reduced. In this study, C_3 was set to 0.05 for aethalometer measurements. Using higher values caused the size-related portion of the PMF to dominate due to the larger number of size classes, leading to additional size modes lacking clear physical interpretation. In some configurations, the contributions associated with traffic emissions and residential biomass burning became unrealistically small. Similar issues concerning the mass of the traffic factor were reported by Forello et al. (2023). Notably, the selected configuration yielded PM_{10} contributions for traffic and biomass burning that are consistent with the method described by Aujay-Plouzeau (2020), which is based solely on aethalometer measurements.

8. During this process, it was necessary to increase the number of factors relative to the initial run, which was based only on size, in order to accommodate factors emerging from the multispectral absorption-driven splitting (e.g., traffic, biomass burning, condensation-mode secondary aerosols). More details on the selection of the optimal number of factors are provided in Sect. S11.

9. The plot of the original and reconstructed time series were examined for each input species to verify whether the selected uncertainty configuration reproduced the original data satisfactorily.

10. Note that α primarily affects the PMF behaviour at low concentrations of a species, whereas C_3 influences the behaviour at medium to high concentrations. This distinction is particularly important for species exhibiting a marked seasonal cycle, such as those related to biomass burning. In such cases, the minimum uncertainty (constant component, see Table S1) should be chosen so that winter and summer conditions are clearly distinguished, i.e. situations in which the species is present or absent in the atmosphere are well separated.

11. The factor uncertainties were finely adjusted at the end of the procedure by scaling them so that the residuals fell within the expected range of ± 3. In this study, an additional 20 % increase in all C_3 values was required. The coefficients were scaled accordingly rather than introducing an additional parameter ('Additional model uncertainty') in EPA PMF 5.0. The C_3 values reported in Table S1 include this factor and their reported digits are approximated to ± 0.05 for clarity.

The final values for the parameters A, α, and C_3 are shown in Table S1.

Table S1: Parameters for the calculation of the overall uncertainty following the same framework as in Vörösmarty et al. (2024). The total variable PM_{10} and the size channels at d > 6 ţm are set as weak variables in PMF; the corresponding values in this table have already been multiplied by 3.

	PM_{10}	Delta-C	NeBC(470–950 nm)	d < 2 ţm	2 ţm < d < 6 ţm	d > 6 ţm
A	3	1	1	1	1	1
α	0.01	0.01	0.01	0.01	0.01	0.01
C_3	0.35	0.05	0.05	0.10	0.35	0.45

It may be noted that:

– The uncertainty assigned to the largest size channels (d > 6 ţm) is relatively high. This reflects the low number concentration of large particles and their 'shot' nature, which introduces greater variability when considered from a Poisson-based perspective (Sect. S2.1). Indeed, these bins typically contain a few peak values emerging from a background of zeros, whose frequency can reach up to 30 %. Consequently, these size channels, together with the total variable PM_{10}, were classified as weak variables in the PMF configuration to prevent them from exerting excessive influence during subsequent tests. During the testing phase, as suggested in previous studies (e.g., Zhou et al., 2004; Thimmaiah et al., 2009; Zhou et al., 2005b), an alternative approach was also evaluated in which the largest size bins were grouped (in sets of three to five, depending on particle

size) to mitigate issues associated with low particle counts and to improve the signal-to-noise ratio (SNR). Although bin grouping effectively increased the SNR, it hindered the separation of the two coarse factors (desert dust and local resuspension). For this reason, this approach was not adopted in the final configuration.

– The NeBC uncertainties used in this study are lower than those reported in some previous works (e.g., Forello et al., 2019; Rigler et al., 2020). In particular, Forello et al. (2023) applied an uncertainty as high as 50 % for b_{abs} to avoid convergence issues when coupling absorption data with chemical data in the PMF. With such high uncertainty values, combined with the smaller number of optical variables relative to chemical species, the NeBC information effectively follows the factorisation rather than contributing to it. In contrast, the present approach aims to ensure that both spectral absorption and volume size distribution contribute to determining the final solution. Consequently, the uncertainty values adopted here should not be interpreted as strict measurement uncertainties, but rather as weighting parameters used to balance the influence of the different input variables on the Q metric.

S8 Seasonal splitting

As part of this study, we investigated whether seasonal PMFs could improve RASPBERRY source identification. The profiles obtained separately for each season (not shown) differ significantly from the annual PMF, particularly for winter and summer. For instance, while the winter PMF identifies the same profiles as the annual PMF, it fails to correctly assign PM_{10} mass contributions to each factor. Specifically, the traffic emissions and secondary droplet mode factors are approximately half of those obtained with the annual PMF, whereas the secondary condensation and dust factors are 25–30 % higher. These discrepancies contradict the results from the chemical PMF. We attribute this behavior to the overlap of several sources during winter, the persistence of their emitted particles in the atmosphere, and the modulation of their concentrations by meteorological conditions. Indeed, at the particular study site, meteorology is a main driver of PM_{10} concentrations and a confounding factor. For example, strong temperature inversions can increase pollutant concentrations at the surface, while Foehn winds can dramatically decrease them, introducing strong correlations between species. This large rotational ambiguity is particularly evident in the G-space PMF plots, where clear edges are visible especially for fine modes and cannot be mitigated by F-peak rotations. Conversely, in the summer PMF, certain factors such as the droplet mode and biomass burning are almost absent. In place of the latter, for instance, a factor emerges with a large Delta-C and a flat VSD, which deviates significantly from the annual biomass burning profile. As a consequence, contributions differ as well: traffic emissions are 50 % higher compared to the annual PMF for the same season, residential biomass burning is 150 % higher, and the separation between desert dust and local coarse particles is poorer. As a confirmation of our hypothesis, the spring and autumn PMFs are more consistent with the annual results. Indeed, during these transitional seasons, various emission sources alternate, enabling better factor separation.

S9 Details on RASPBERRY+EVLS

For every sample collected at time t_i, effective variance least squares (EVLS) retrieves the contribution of factor k, g_{ik}, by minimising the following metric (Watson et al., 1984, note that typographical errors are present in Chen et al. (2025)):

$$Q' = \sum_{j=1}^{m} \frac{\left(x_{ij} - \sum_{k=1}^{p} g_{ik}\, f_{kj}\right)^2}{u_{ij}^2 + \sum_{k=1}^{p} (g_{ik}\, u_{f_{kj}})^2} \tag{S3}$$

where u_{ij} represents the uncertainty of species j measured at the receptor at time t_i, and $u_{f_{kj}}$ represents the uncertainty of species j in factor profile k, which is derived from the interval ratio obtained from the DISP test (half of the interval is adopted here as the standard uncertainty). Therefore, compared with a simple least-squares regression of the measured species against known profiles weighted by the measurement uncertainty (as performed in RASPBERRY), the EVLS metric also accounts for uncertainties in the source profiles.

The problem is solved iteratively:

- In iteration 'zero', the profiles f_{kj} are taken from the PMF solution and their respective uncertainties $u_{f_{kj}}$ are set to zero. Under these conditions, the solution (g_{ik}) is identical to that obtained with the standard PMF and RASPBERRY.
- In the subsequent iterations, the previously estimated g_{ik} values and the profile uncertainties $u_{f_{kj}}$ are included in Eq. S3 to provide updated weightings, and new contributions g_{ik} are calculated.
- The iterative process terminates once convergence is reached, e.g. when the relative change in the squared sum of the pairwise differences between the new and previous contributions falls below 10^{-5}.
- Finally, the uncertainties associated with the g_{ik} values are calculated as the square roots of the diagonal elements of the covariance matrix used in the inversion.

The method is implemented in RASPBERRY using the R code provided by Dai and Hopke (2025). It is also applied in combination with the chemical PMF results to derive uncertainties in the source contributions obtained from the chemical source apportionment.

When calculating daily average concentrations from hourly RASPBERRY retrievals, the corresponding uncertainties are estimated using the root-mean-square of the hourly uncertainties, assuming that the latter are strongly correlated within each day due to dominant systematic contributions. This approach provides a conservative estimate and avoids an artificial reduction of the uncertainty through averaging.

Since EVLS minimises a different metric from that used in PMF (and in RASPBERRY), the resulting contributions may also differ, sometimes leading to an improved reconstruction of the observed species concentrations (Chen et al., 2025). Figure S3 illustrates a comparison between the retrievals obtained with RASPBERRY and RASPBERRY+EVLS. Differences are generally very small, with R^2 values of 1 and regression coefficients very close to the 1:1 line. Slightly larger, although still negligible, differences are observed for secondary factors.

The comparison of uncertainties derived from the two methods is more complex. Figure S4 compares the uncertainty associated with RASPBERRY, defined as half of the interval of the PM_{10} profile component from the PMF DISP test, with the uncertainty associated with RASPBERRY+EVLS, which is calculated by propagating both profile uncertainties (across the components of all species) and measurement uncertainties. The estimates obtained from the two methods differ substantially, and their comparison depends on the specific factor considered.

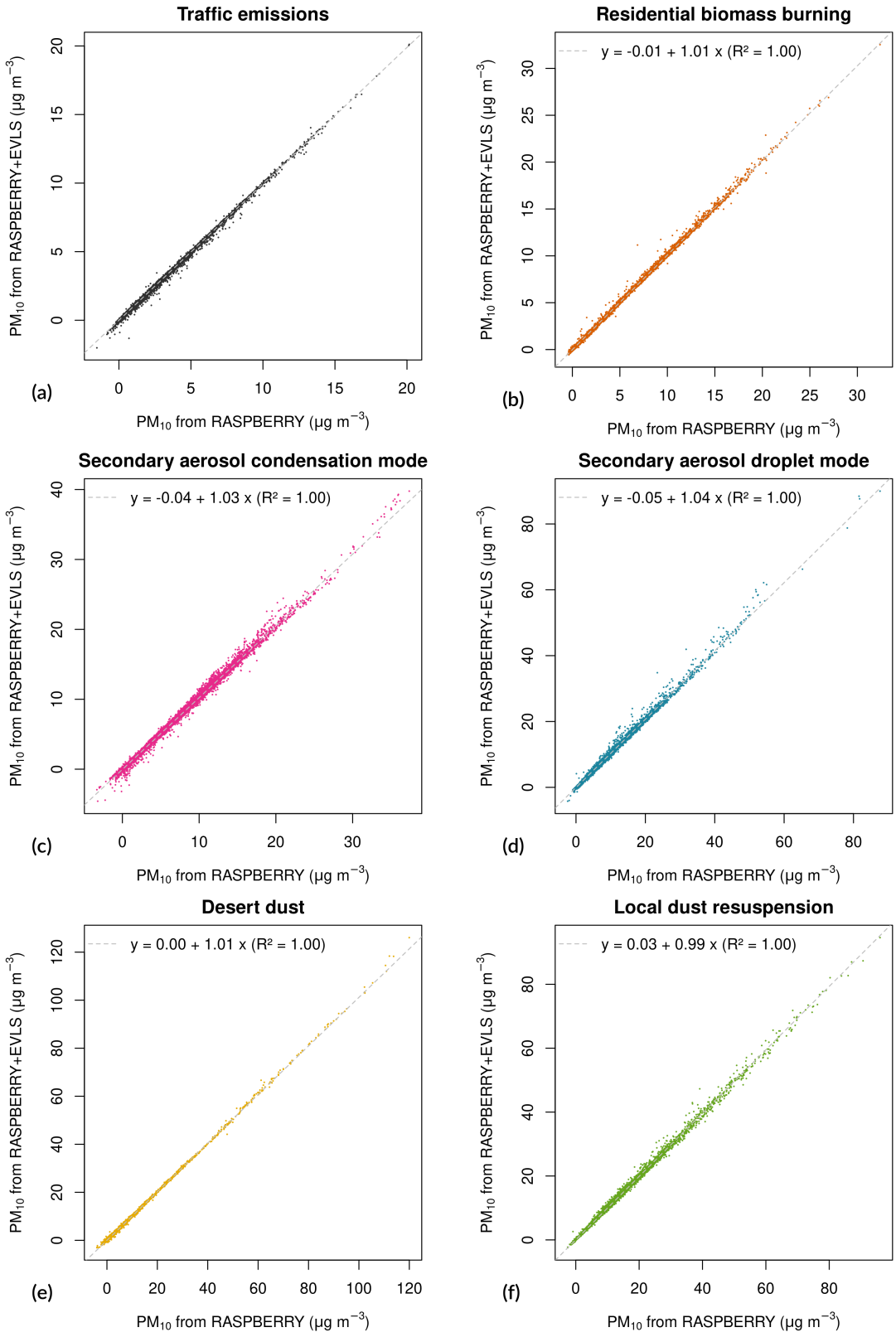

Figure S3: Comparison of PM_{10} retrievals obtained with RASPBERRY and RASPBERRY+EVLS for the different factors.

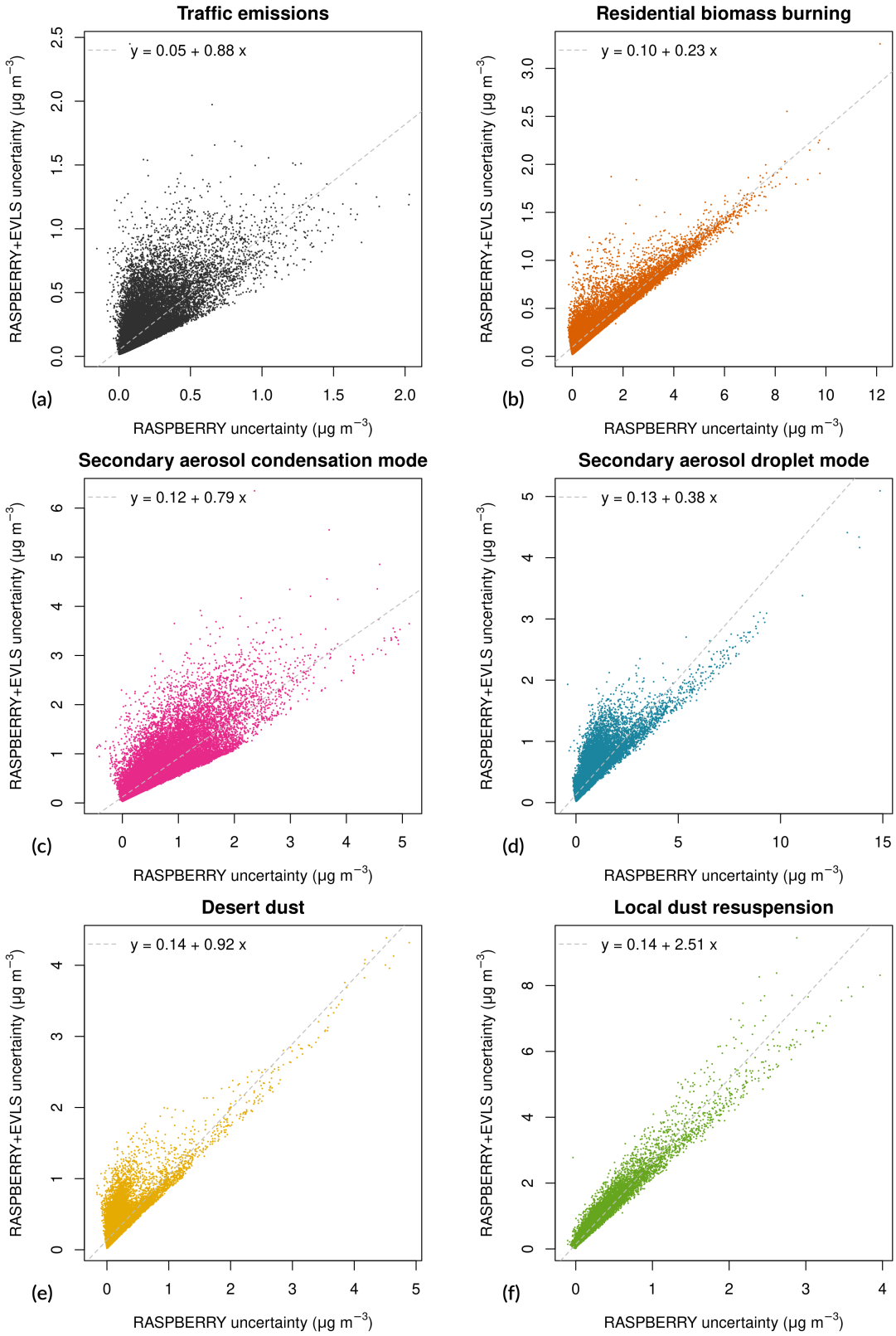

Figure S4: Comparison of uncertainties estimated for RASPBERRY and RASPBERRY+EVLS retrievals. In the first case, half of the interval of the PM_{10} profile component from the PMF DISP test is used here as the uncertainty associated with RASPBERRY for each factor. In the second case, the uncertainty associated with RASPBERRY+EVLS is calculated using the EVLS method by propagating both profile and measurement uncertainties.

S10 Selection criteria for optimal number of factors in the chemical PMFs and associated quality metrics

Factorisations with up to seven factors were explored for both chemical PMFs, based on water-soluble ions combined with EC/OC and levoglucosan (dataset 1), or ions and metals (dataset 2). In both cases, six-factor solutions were selected as optimal.

For chemical dataset 1, the 5-factor PMF solution results in traffic emissions and crustal sources merging, likely due to their interaction through dust resuspension. Conversely, the 7-factor solution increases the $\frac{Q_{true}}{Q_{exp}}$ ratio and leads to $NH4^+$ separating into its own factor, with no physical reasons. The selected 6-factor solution (Fig. S5) is achieved with 100 runs, yielding $Q_{rob} = 1065$ (same value for Q_{true}) and a $\frac{Q_{true}}{Q_{exp}}$ ratio of 1.5. The PM_{10} is reconstructed with an R^2 of 0.8, an intercept of 4.0 $\mu g\,m^{-3}$ and a slope of 0.7. All strong species are reproduced with $R^2 > 0.9$. To better distinguish the biomass burning factor, three constraints are applied: levoglucosan is maximally pulled up in the biomass burning factor and set to zero in the traffic and sodium chloride (road salting) factors, resulting in a dQ increase of just 0.37 %. The constrained DISP test reveals no swaps or decreases in Q. The BS test is conducted with 100 bootstraps, a minimum correlation R-value of 0.6, and a block size of 30. Corrections to the erroneous block size value suggested by EPA PMF5 are applied based on Patton et al. (2009) and Bhandari et al. (2022), with the final value determined using the 'b.star' routine from the 'np' R package (Hayfield and Racine, 2008). All boot factors match their respective base case factors 100 %, except for the traffic factor (91 % match, with 9 % attributed to the crustal factor) and the crustal factor (97 % match, with 3 % attributed to the sulfate-rich factor). These slight mismatches can be physically justified by the fact that traffic and crustal sources are linked through resuspension, while sulfates are often associated with the crustal component during summer. BS-DISP is performed as well, by actively displacing the most representative species among the strong ones (EC, NO_3^-, SO_4^{2-}, Cl, and levoglucosan). The test shows no significant decrease in Q (< 0.5 %), however, swaps are already observed at $dQ^{max} = 0.5$ between the road salting and biomass burning factors. This is likely due to their concurrently high values during winter and the limited number of measured species analysed, indicating that dataset 1 is affected to some extent by rotational ambiguity.

For chemical dataset 2, the 5-factor solution results in nitrate and part of sulfate merging into a single factor, while some sulfate and crustal elements combine into another. Using 7 factors, the Q value remains comparable to that of the 6-factor solution, however Cd is unphysically separated into its own factor. The 6-factor solution (Fig. S6) is therefore selected, yielding $Q_{rob} = 9704$, $Q_{true} = 9725$ and $\frac{Q_{true}}{Q_{exp}} = 2.3$. The BS test is conducted using 100 bootstraps with a minimum correlation R-value of 0.6 and a block size of 39. All factors are correctly mapped in over 98 % of cases, with only minor swaps observed between the sulfate- and nitrate-rich factors. The DISP test reveals no swaps or decreases in Q. BS-DISP is performed by actively displacing the following strong and representative species: Fe, Ni, Cu, Cl^-, NO_3^-, SO_4^{2-}. No swaps and no significant decreases are observed in Q ($dQ < 0.2$ %). The measured PM_{10} is reconstructed by the PMF with an R^2 of 0.9, an intercept of 1.4 $\mu g\,m^{-3}$ and a slope of 0.88. Most strong species are reproduced with $R^2 \geq 0.9$.

It should be noted that for both datasets, additional constraints could be applied to pull down or set to zero Ca^{2+} and Mg^{2+} concentrations, clear markers of resuspended dust, in the 'traffic emissions' profile. This adjustment would redefine the 'traffic' profile as 'fossil fuel' or 'traffic exhaust', i.e. without any non-exhaust component. The choice is subjective, with both advantages and disadvantages depending on the approach. Considering that Palas Fidas 200 is only sensitive to particles with diameters >0.18 μm, and that the contribution of traffic in a broader sense (exhaust and non-exhaust) may be more relevant in a policy perspective, we choose not to introduce additional constraints on Ca^{2+} and Mg^{2+}, and keep the partial correlation between crustal matter and traffic emissions as it emerges from the PMF. For consistency, a similar logic is used in the physical PMF.

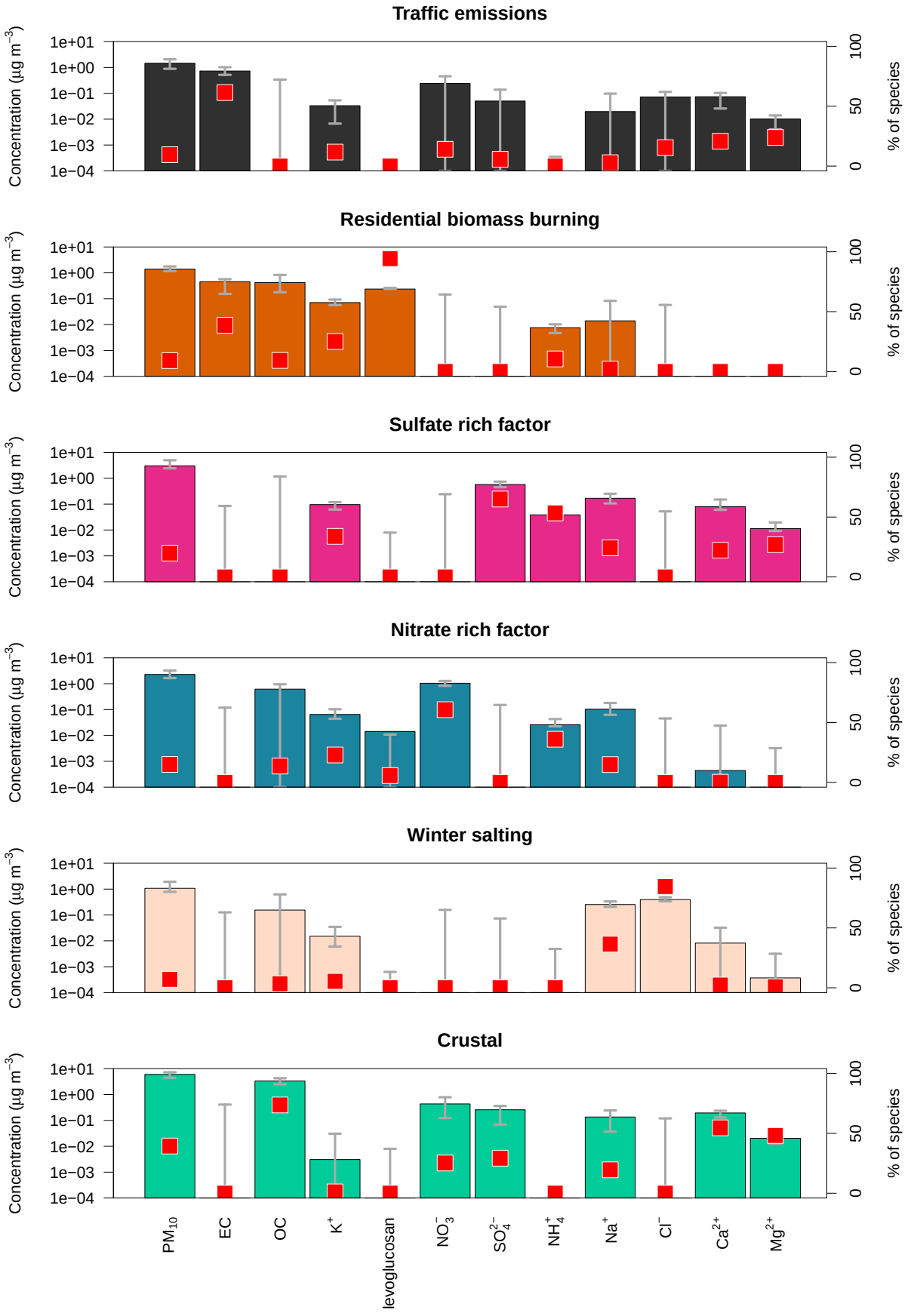

Figure S5: PMF solution profiles obtained with dataset 1 (anion/cation, EC/OC and levoglucosan). Bars represent the absolute mass contribution of each species in each factor (left y-axis), while the small squares represent the percentage contribution of each factor to each species (right y-axis). The error bars depict the $dQ^{max} = 4$ range of the DISP test.

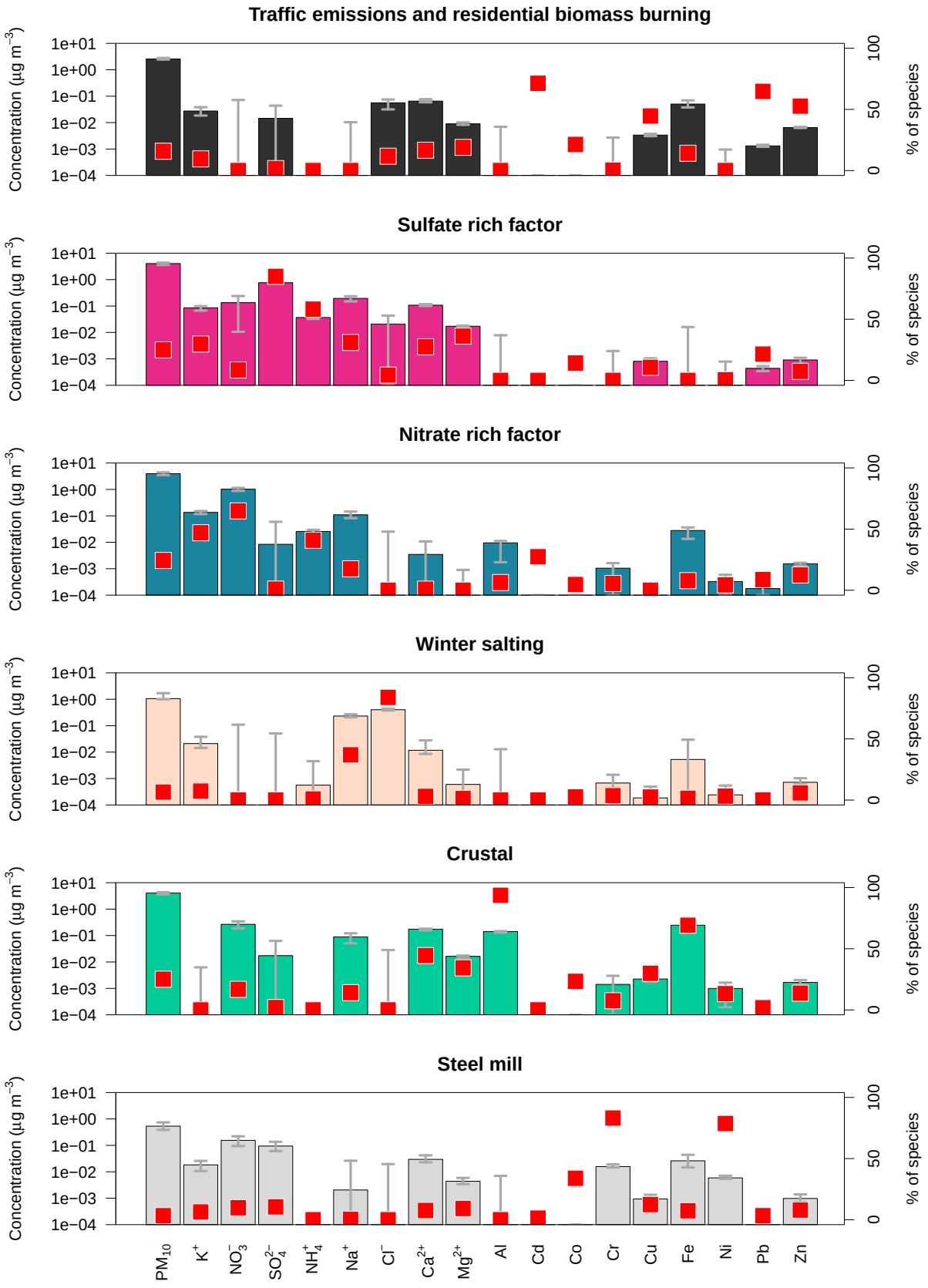

Figure S6: PMF solution profiles obtained with dataset 2 (anion/cation and metals).

S11 Selection and fine-tuning of the optimal physical PMF solution

4000 samples, each containing 70 species and the total variable PM_{10}, were given as input to the PMF. 55 species were classified as strong variables: Delta-C, NeBC(470–950 nm) and volume size distributions at diameters <6 ţm, as described in Sect. S7. No missing values were present in the input dataset. The remaining size bins were set as weak. Solutions were explored with a variable number of factors up to 7, with the 6-factor solution being considered the best. This choice was based on the following criteria: (i) the physical interpretability of the profiles; (ii) the $\frac{Q_{true}}{Q_{exp}}$ ratio; (iii) the shape and the range of the scaled residual distribution. The 5-factor solution showed a higher $Q \sim 2$, with $\frac{Q_{true}}{Q_{exp}}$ for Delta-C reaching 25, due to the merging of traffic emissions and residential biomass burning factors. The 7-factor solution yielded an overall $\frac{Q_{true}}{Q_{exp}}$ ratio of 1.2, and an additional factor with a modal diameter of approximately 1 ţm. Interestingly, a similar intermediate mode has been observed in previous studies (e.g., Bernardoni et al., 2017), and has been linked to various sources, including coal combustion (Pakkanen et al., 2001; Salma et al., 2005), traffic-related emissions as a secondary maximum (Gu et al., 2011), resuspension (Sowlat et al., 2016), and primary emissions from heavy-duty vehicles (Rivas et al., 2020), or even to inconsistencies between optical and aerodynamic diameter determinations (Vu et al., 2015). In our study, for the 7-factor solution, this factor shows strong correlations with many others, complicating its physical interpretation. Even more importantly, its inclusion leads to a significant reduction in the biomass burning contribution, despite the profile of the intermediate factor showing zero NeBC concentration or Delta-C. Consequently, the 7-factor solution was discarded in favour of the more interpretable 6-factor solution.

To fine-tune the 6-factor solution, 9 samples were excluded due to their $\frac{Q_{true}}{Q_{exp}}$ ratio being ≥ 5. Curiously, these samples were not related to events characterised by high PM_{10} concentrations, but rather by quite low concentrations, as also found by Bhandari et al. (2022). This suggests that removing these low values likely enabled the PMF to find a better rotation. The resulting overall $\frac{Q_{true}}{Q_{exp}}$ ratio is 1.4 ($Q_{exp} = 195670$) and single species $\frac{Q}{Q_{exp}}$ generally within 1–2 except the largest size bins with values slightly > 2 (the uncertainty was not further tuned for those classes in order not to complicate the configuration). Q_{true} and Q_{rob} differ by only 0.8 %, meaning that outliers have almost no effect. After the base run, two constraints are applied: the NeBC at 880 nm is pulled down in the local coarse dust resuspension and in the secondary condensation mode factors, to enhance separation from the combustion-related factors (i.e., traffic emissions and residential biomass burning). This refinement of the optical absorption properties, also employed in other works (Savadkoohi et al., 2025), is based on the negligible EC concentrations in the crustal and sulfate-rich modes in the chemical PMF and transfers some mass, likely due to resuspension, from the local coarse factor to the traffic emission one. The constraint at 880 nm is sufficient to reduce NeBC levels at the other aethalometer wavelengths. Both constraints increase Q by only 0.25 %. The bootstrap (BS), displacement (DISP) and BS-DISP tests were performed. The BS test has been applied with 100 runs, minimum correlation value 0.6 and block size 130. In the BS-DISP tests, only a few representative species were set as actively displaced due to the already high number of samples, i.e. Delta-C, NeBC(880 nm), and VSDs at diameters of about 200 nm, 500 nm, 2 ţm and 6 ţm (this latter is the largest size bin set as strong variable). Zero swaps were detected in all tests, the boot factors were assigned in 100 % of the cases to their respective base factors, and no decreases in Q were found in the DISP and BS-DISP tests. This shows that the physical PMF is rotationally very stable. The total variable, PM_{10}, is reconstructed with $R^2 = 0.97$, intercept -0.99 ţg m^{-3} and slope 1.07. After the CMB-like extrapolation of the whole dataset, as explained in Sect. 3.2 of the main text, the metrics of the measured/reconstructed PM_{10} concentrations remain similar, with $R^2 = 0.97$, intercept -0.88 ţg m^{-3} and slope 1.06. All optical absorption and dimensional 'species' show good reconstructions ($R^2 > 0.9$), except for the 6 largest sizes ($R^2 \sim 0.6$).

S12 Supporting materials on RASPBERRY results

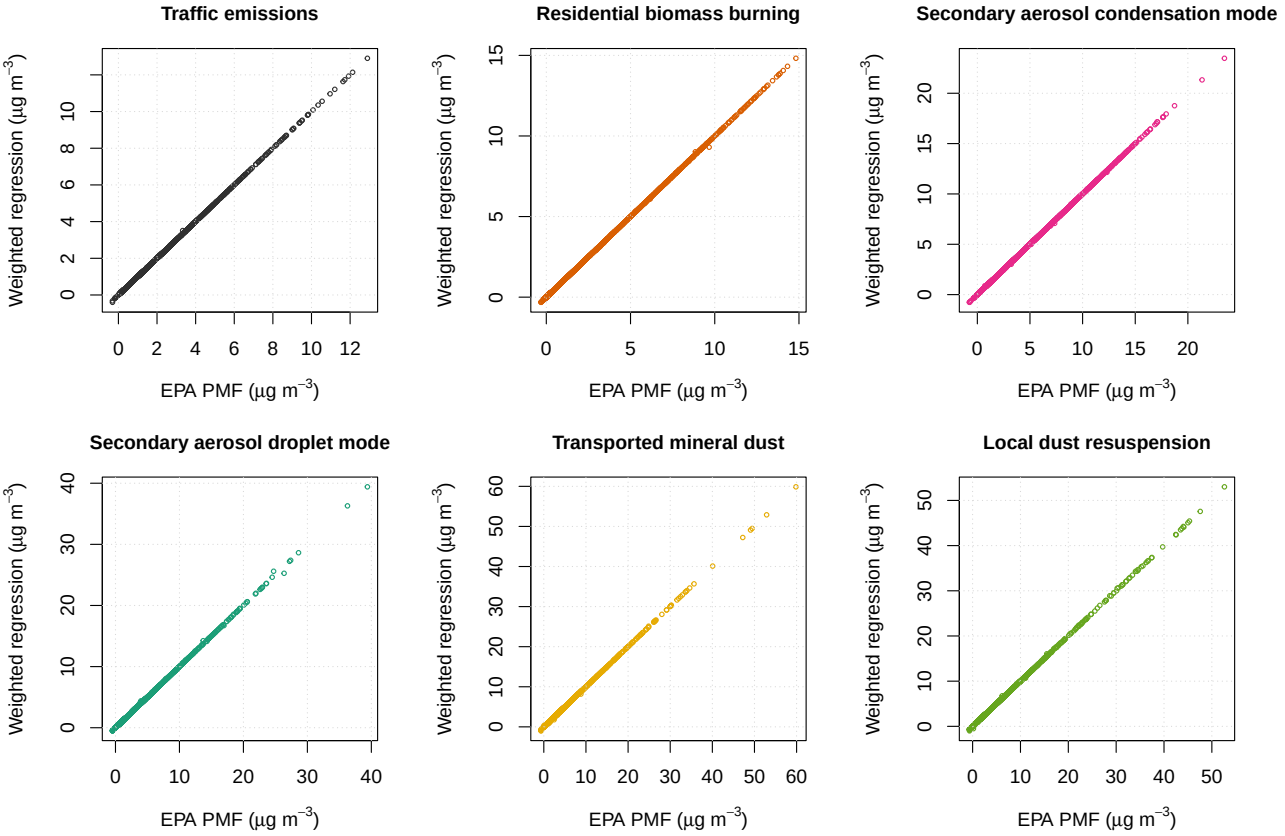

Figure S7: Consistency check of the results obtained using EPA PMF5.0 (x-axis) and the RASPBERRY inversion matrix technique introduced in this study (Eq. 6 in the main text, y-axis), when applying the same profile matrix derived from the PMF. This test considers only the subset of measurements used as input to the PMF. Minor discrepancies are observed, likely attributable to the robust handling of outliers in EPA PMF or numerical approximation errors.

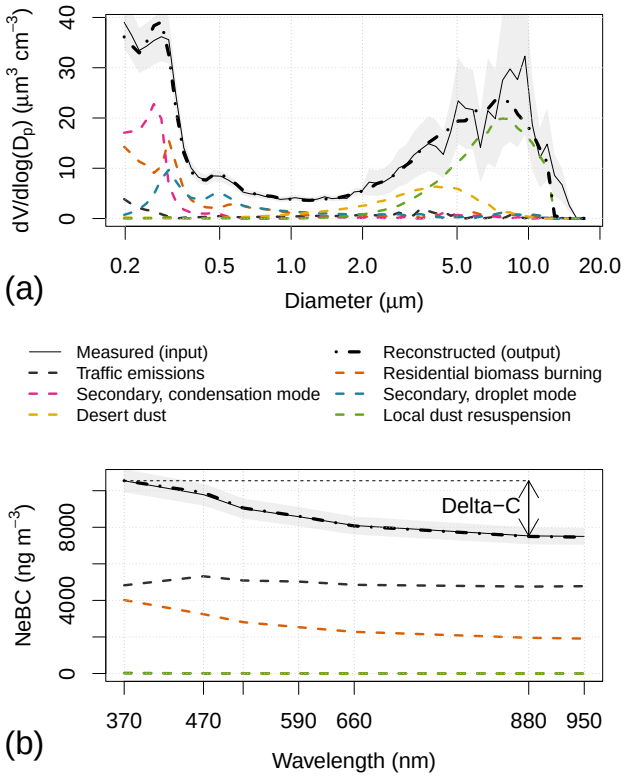

Figure S8: Example of fitting of **(a)** the volume size distribution measured by the OPC (3 January 2020, 21:30 local time) and **(b)** the spectral absorption coefficient expressed as NeBC mass, both shown as continuous black lines. The measurement uncertainty provided to the PMF is plotted as a grey band. The coloured dashed lines represent the six factor profiles identified by the physical PMF, weighted such that their sum (dash-dotted line) best fits the measurements. The same weightings are used to calculate the PM_{10} contributions attributed to each factor. This winter case is here selected because of the high concentrations of both PM_{10} mass (>60 $\mu g\,m^{-3}$) and NeBC.

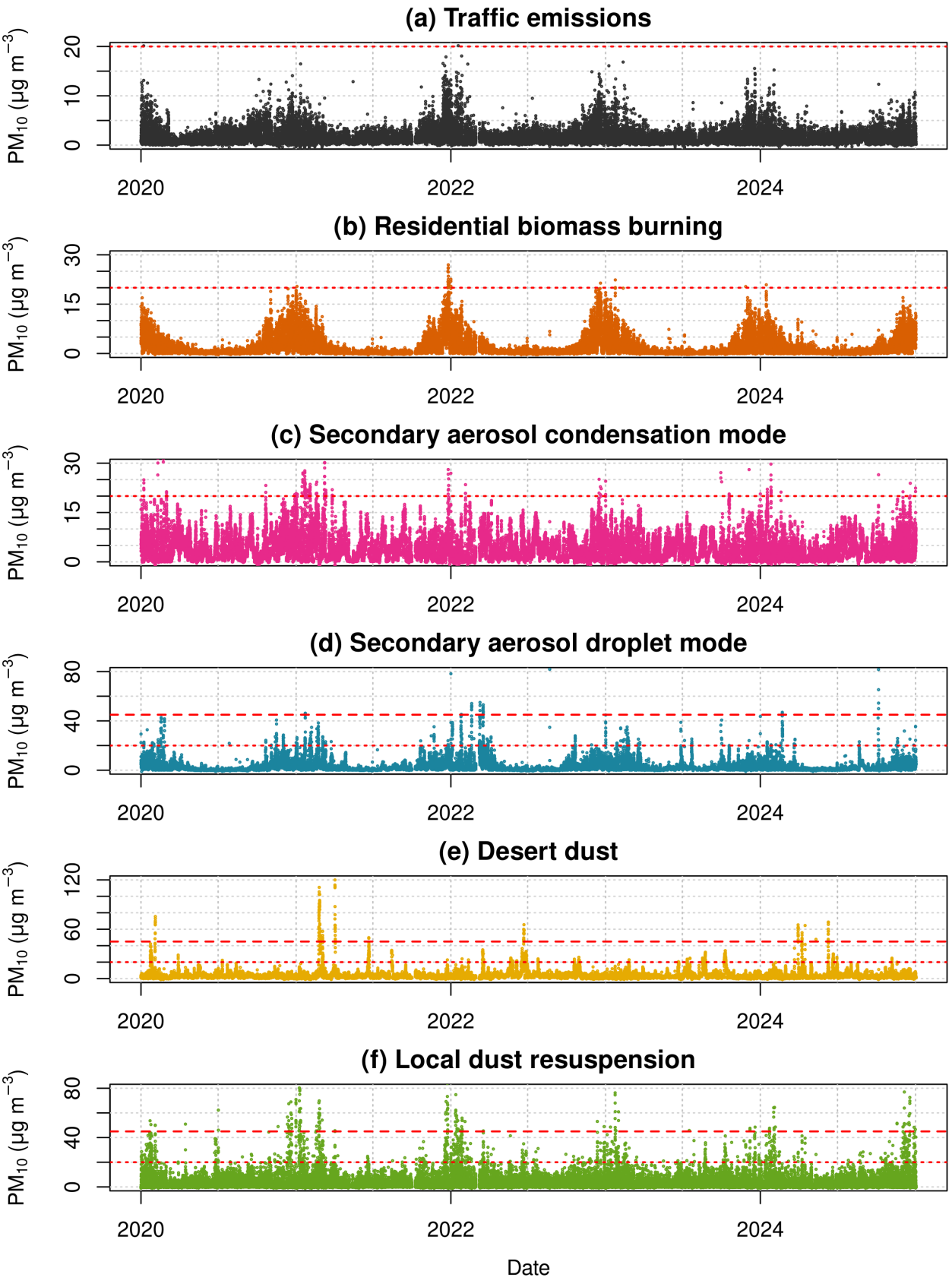

Figure S9: Contribution of each factor to PM_{10} over the entire 2020–2024 period as obtained by RASPBERRY. Red horizontal lines: PM_{10} annual and daily average limit values introduced by the 2024/2881/EC AQ directive.

Table S2: Apparent mass densities of each factor identified by the physical PMF. The uncertainty range is an approximate estimation based on the results of the DISP test, i.e. the $dQ^{max} = 4$ range of the total variable (PM_{10}) mean fraction associated to the factor.

Factor	Density (range), $g\,cm^{-3}$
Traffic emissions	8.9 (8.3–10.1)
Residential biomass burning	3.2 (1.4–3.9)
Condensation mode aerosol	3.6 (3.4–4.4)
Droplet mode aerosol	3.1 (2.7–3.8)
Desert dust	1.3 (1.3–1.4)
Local dust resuspension	0.8 (0.8–0.8)

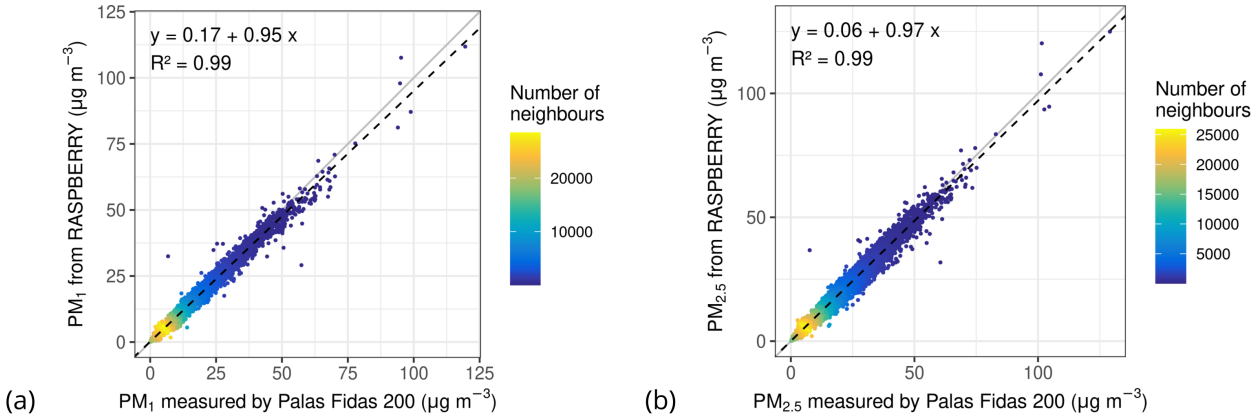

Figure S10: Comparison of measured concentrations (x-axis) and RASPBERRY reconstructions (y-axis) for **(a)** PM_1 and **(b)** $PM_{2.5}$. The reconstructed concentrations are calculated similarly to PM_{10} after reassessing the effective densities of the factors, based on their respective maximum diameters (1 and 2.5 µm instead of 10 µm). The colour scale represents the density of the points.

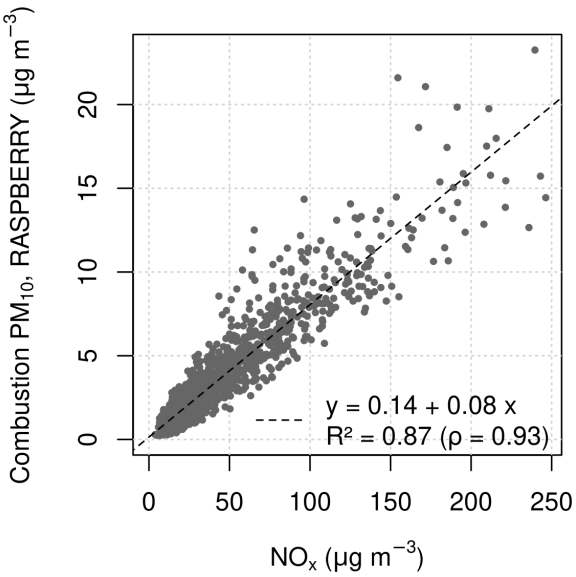

Figure S11: Scatter plot between NO_x (x-axis) measured at Aosta–Downtown and the sum of the PM_{10} contributions from traffic emissions and residential biomass burning determined by RASPBERRY (y-axis).

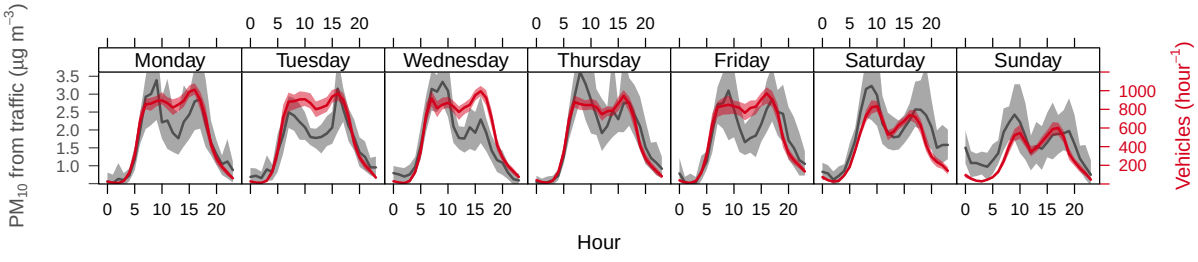

Figure S12: Average daily cycle of PM_{10} concentrations attributed to traffic at Aosta–Downtown (grey, vertical axis on the left) and vehicle counts recorded 500 m to the south (red, vertical axis on the right), during the period 2020–2021. Notice that no meteorological or dilution normalisation was applied to the PM_{10} concentrations.

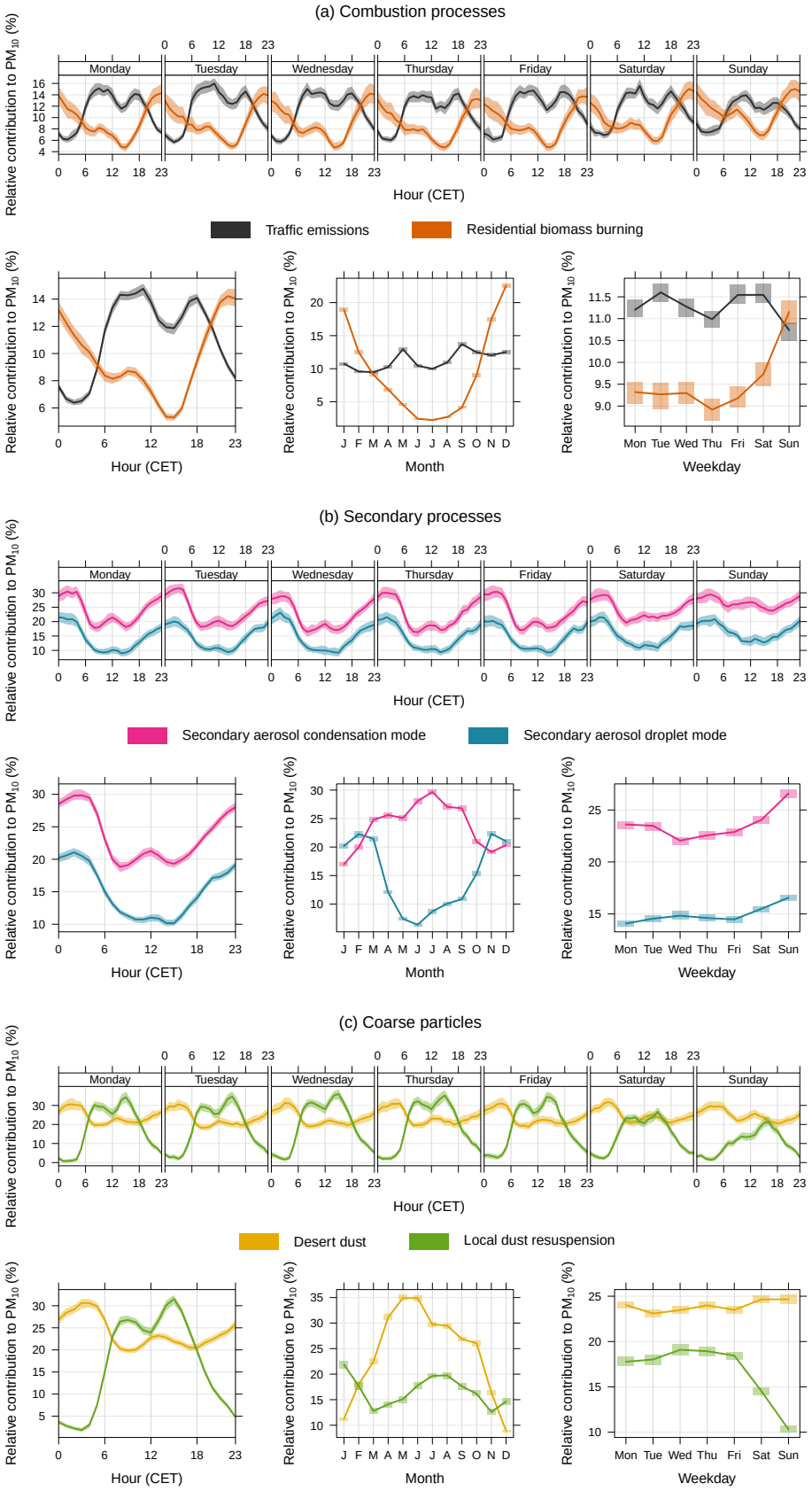

Figure S13: Average percentage contributions to PM_{10} at different temporal scales for factors associated with **(a)** combustion processes, **(b)** secondary processes, **(c)** coarse particles. The bold lines represent the mean contributions, while the coloured areas denote the 95 % confidence interval around the mean.

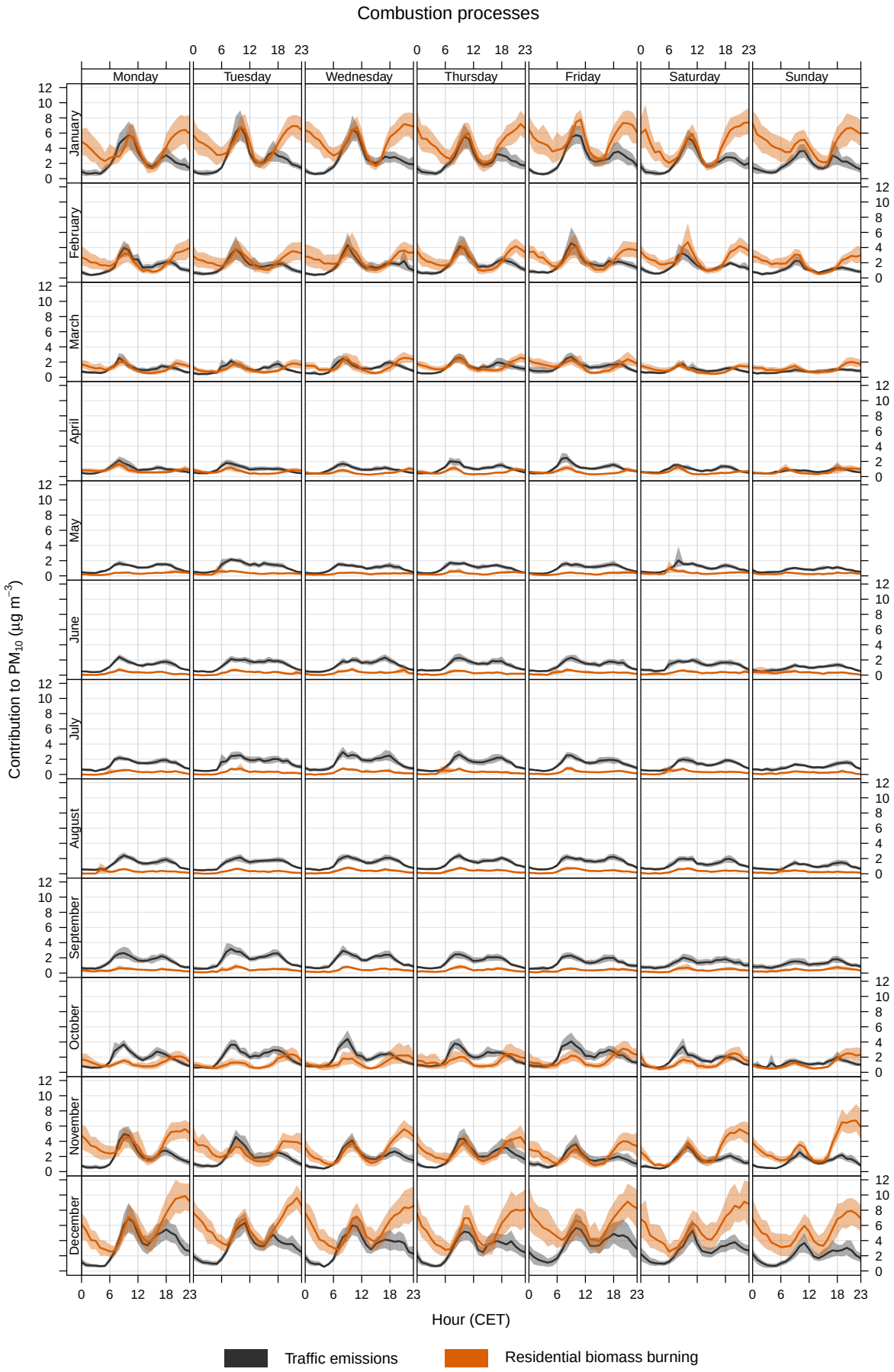

Figure S14: Hourly average contributions to PM_{10} of combustion-related sources split by month and day of the week. The bold lines represent the mean contributions, while the coloured areas denote the 95 % confidence interval around the mean.

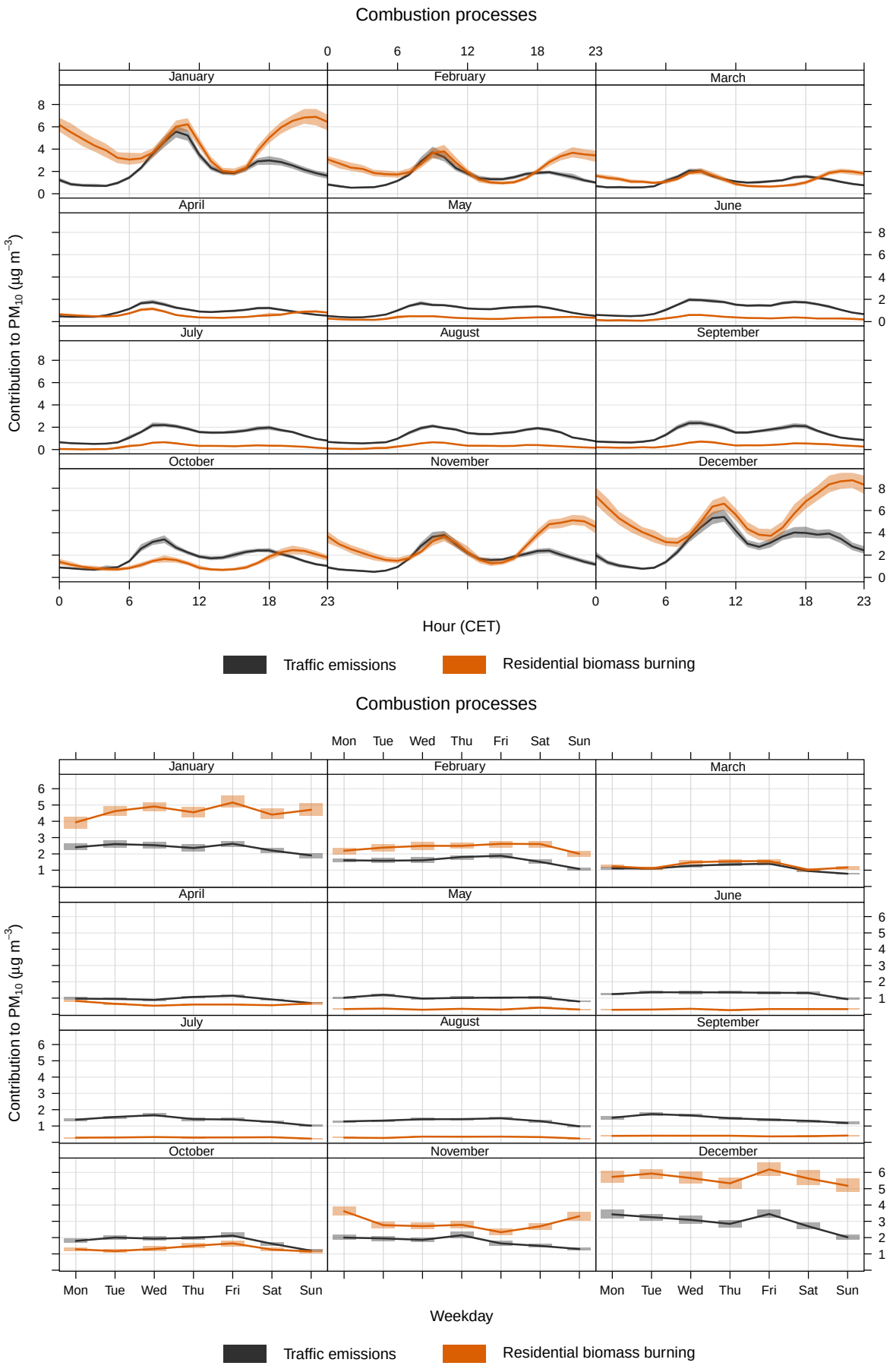

Figure S15: Average contributions to PM_{10} of combustion-related sources split by month as a function of the time of the day and day of the week.

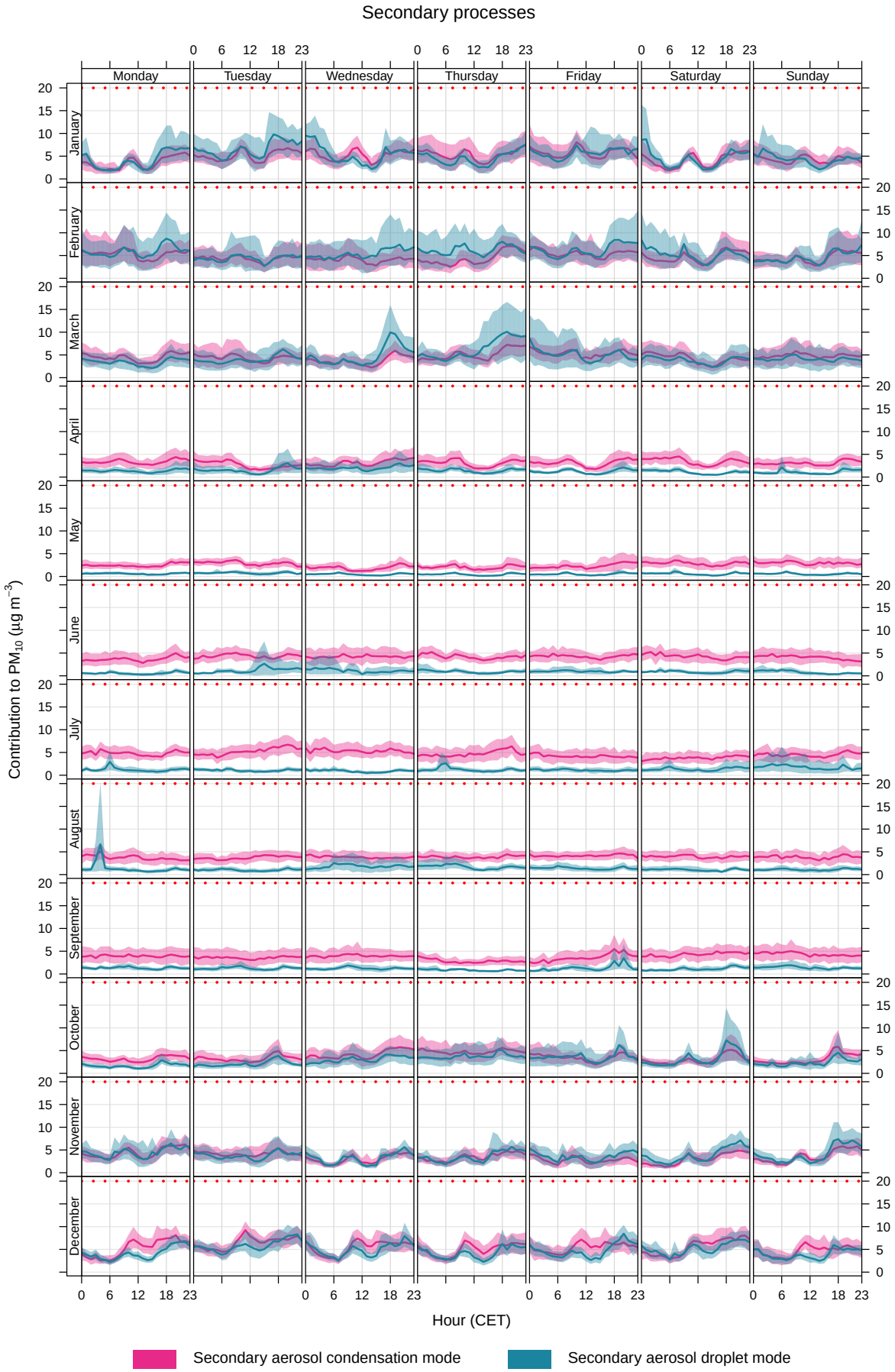

Figure S16: Hourly average contributions to PM_{10} of factors related to secondary particles split by month and day of the week. Red dotted line: PM_{10} (annual average) limit value introduced by the 2024/2881/EC AQ directive plotted as reference.

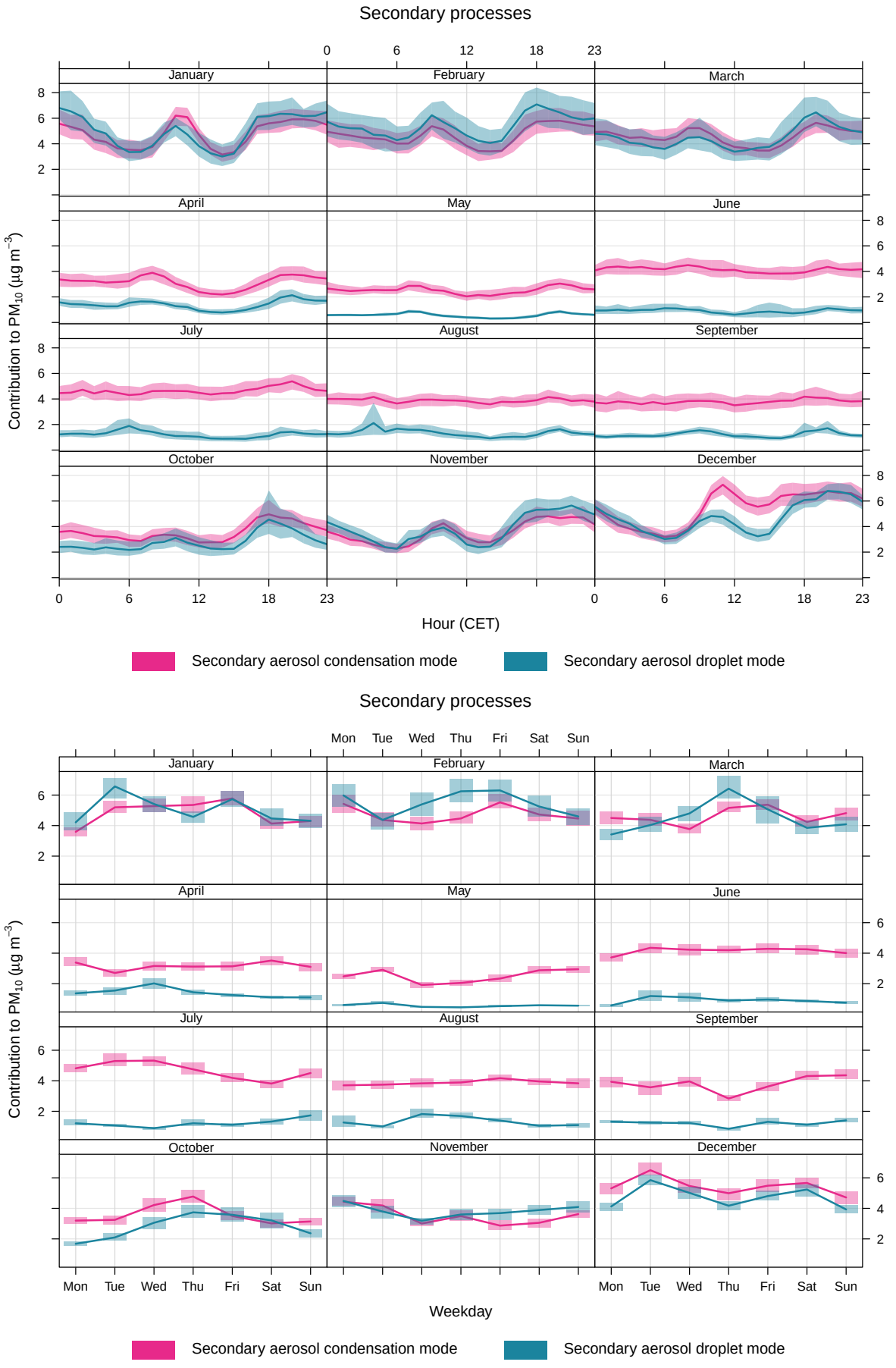

Figure S17: Average contributions to PM_{10} of factors related to secondary particles split by month as a function of the time of the day and day of the week.

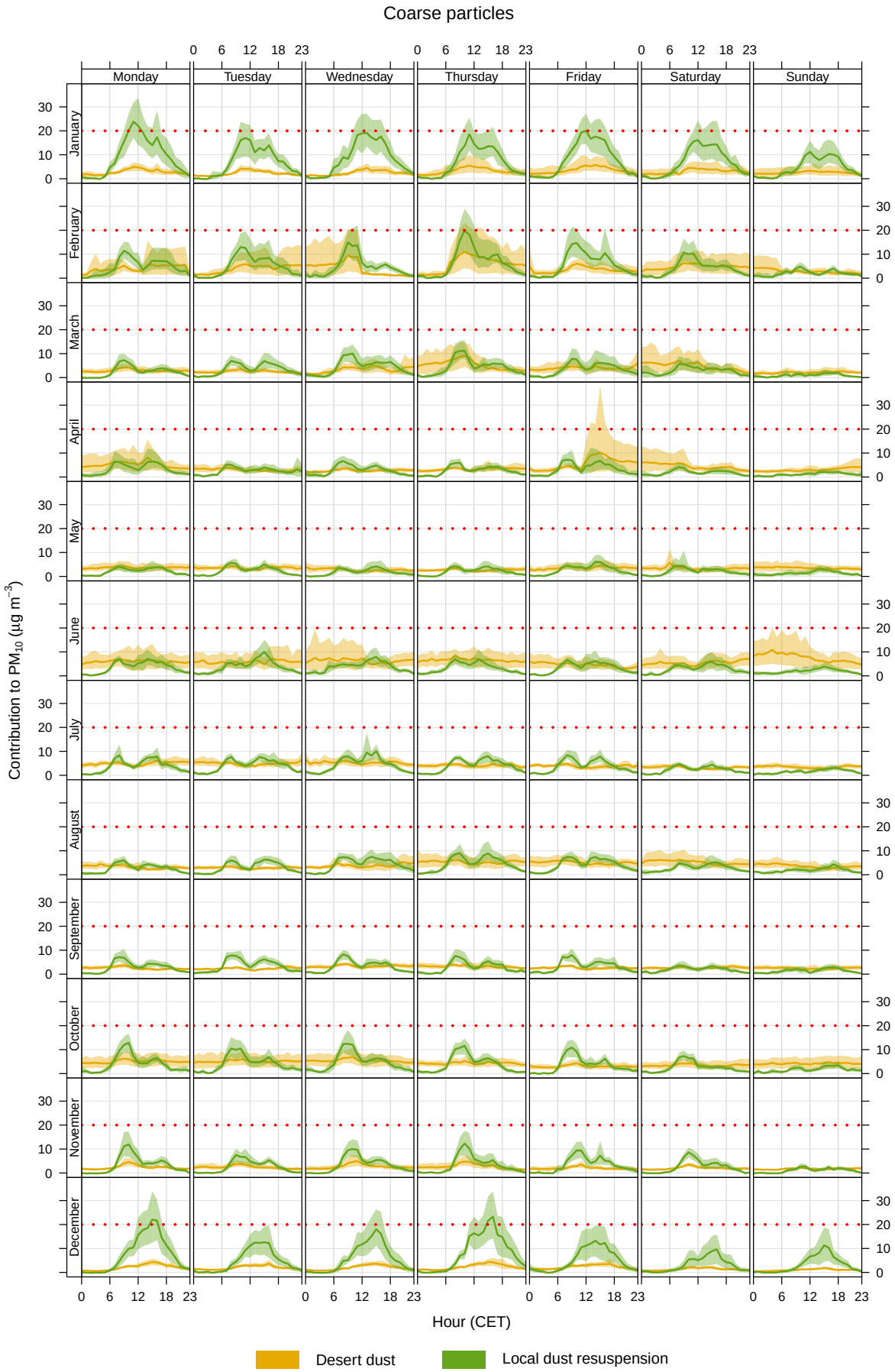

Figure S18: Hourly average contributions to PM_{10} of coarse particles split by month and day of the week. Red dotted line: PM_{10} (annual average) limit value introduced by the 2024/2881/EC AQ directive plotted as reference.

Figure S19: Average contributions to PM_{10} of coarse particles split by month as a function of the time of the day and day of the week. Red dotted line: PM_{10} (annual average) limit value introduced by the 2024/2881/EC AQ directive plotted as reference.

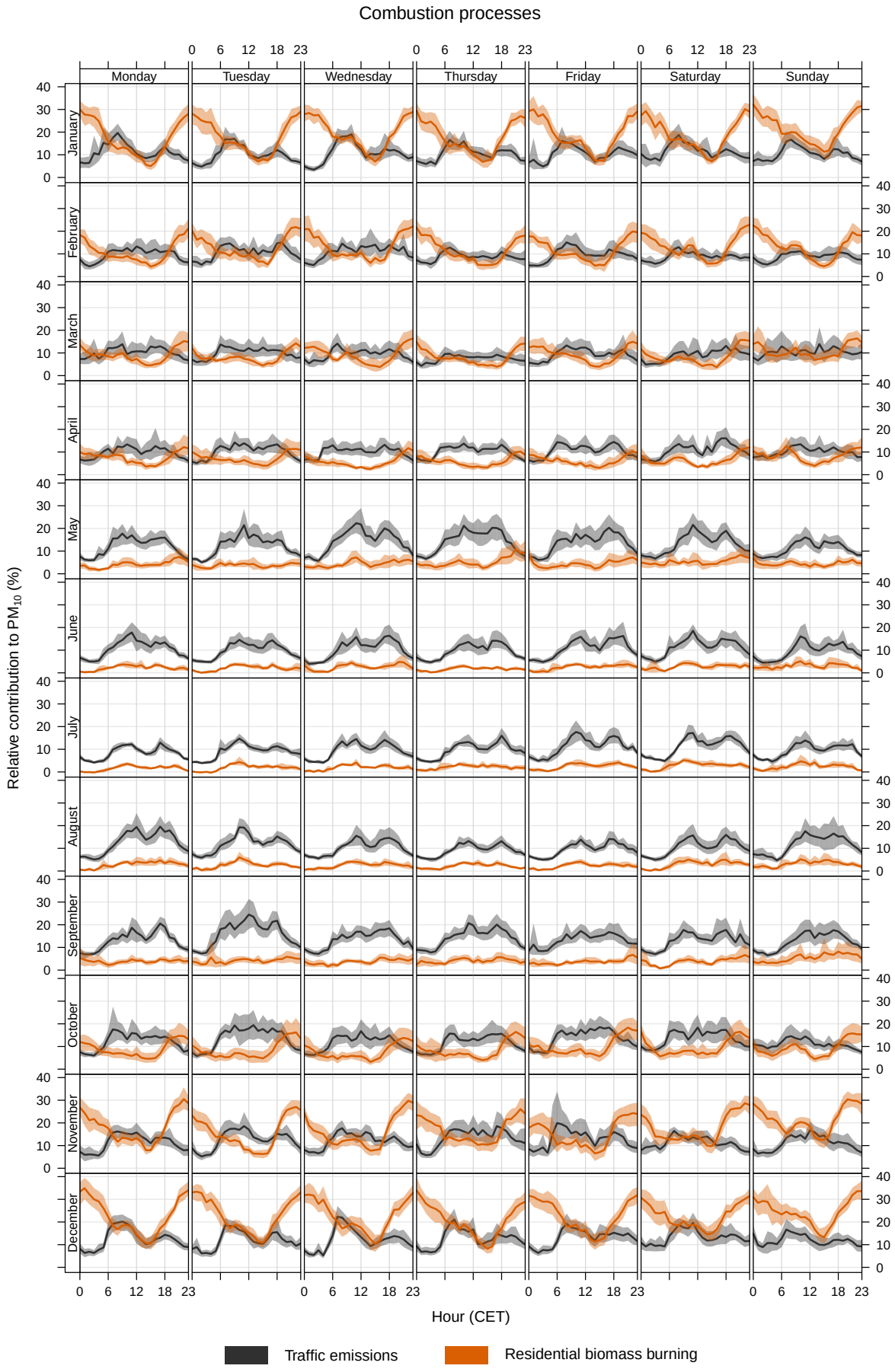

Figure S20: Hourly average percentage contributions to PM_{10} of combustion-related sources split by month and day of the week. The bold lines represent the mean contributions, while the coloured areas denote the 95 % confidence interval around the mean.

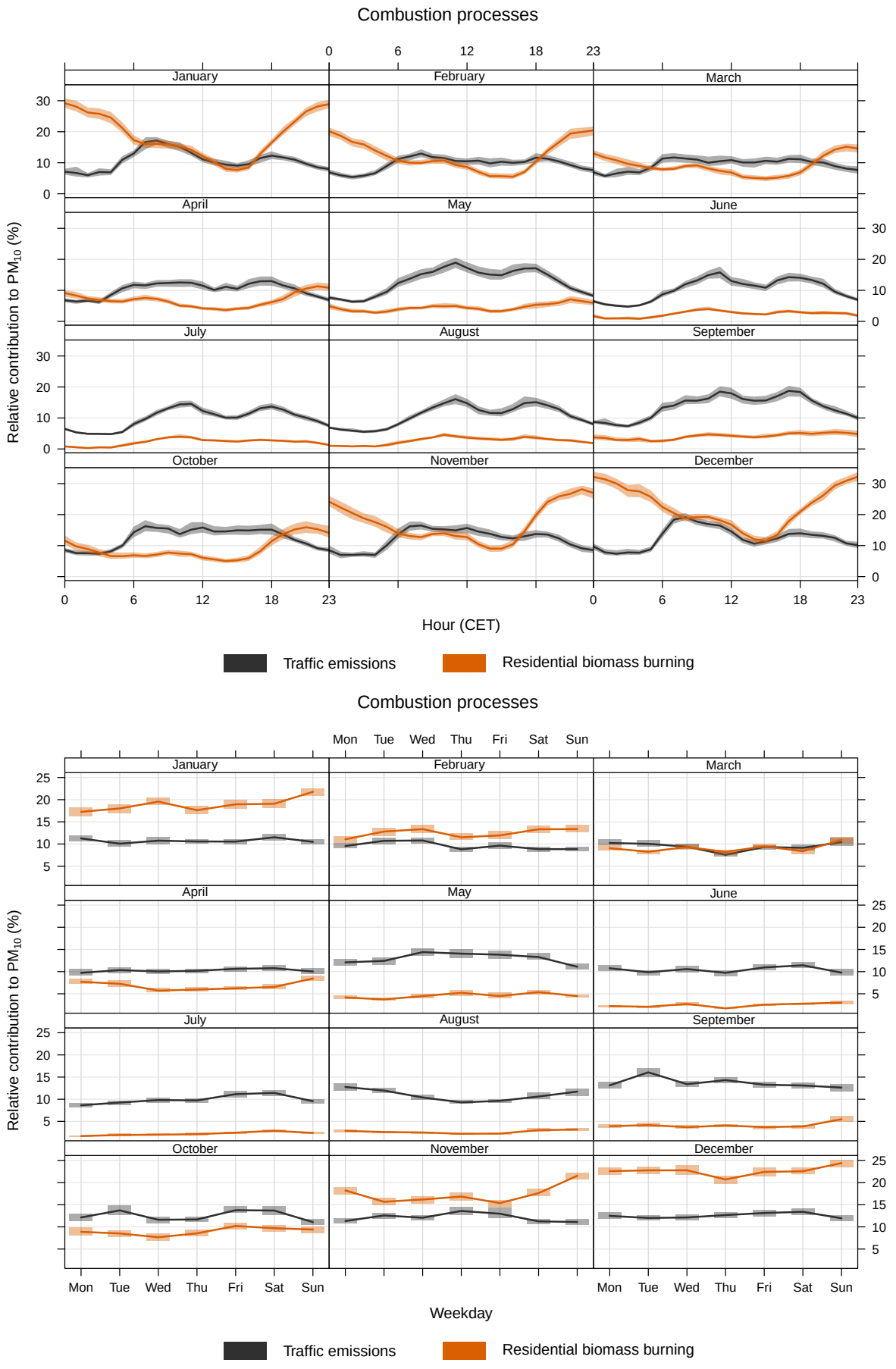

Figure S21: Average percentage contributions to PM_{10} of combustion-related sources split by month as a function of the time of the day and day of the week.

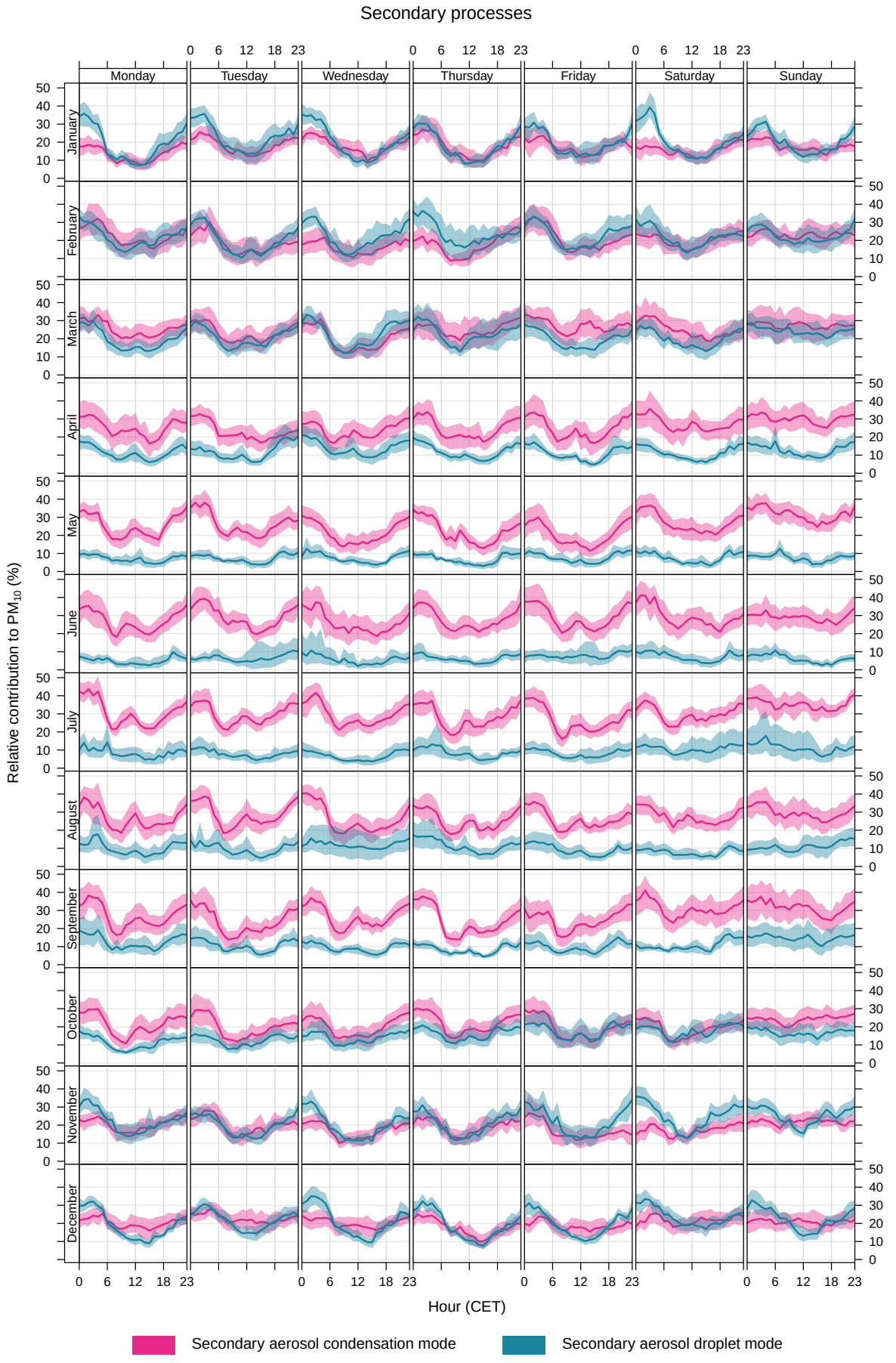

Figure S22: Hourly average percentage contributions to PM_{10} of factors related to secondary particles split by month and day of the week.

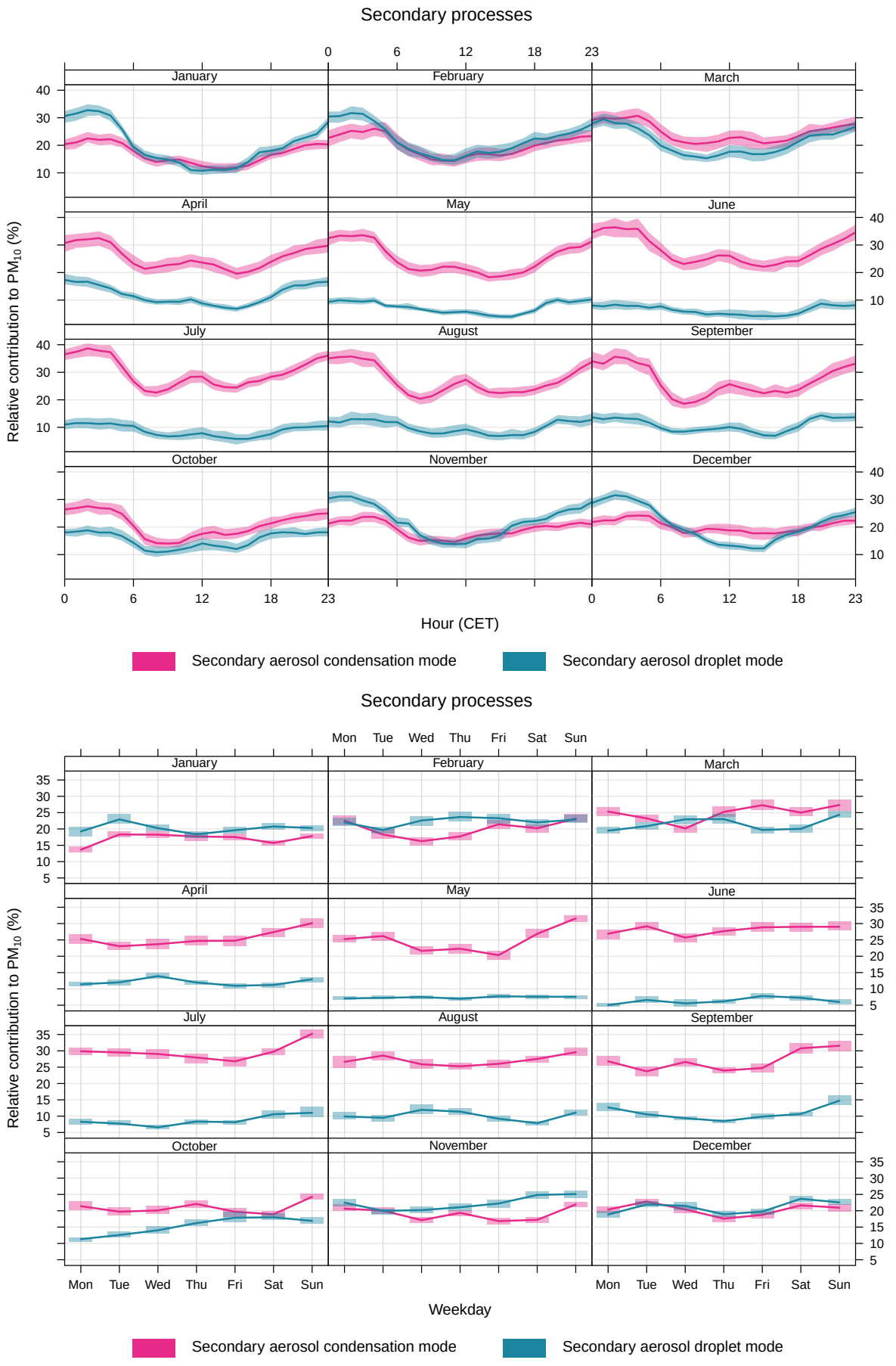

Figure S23: Average percentage contributions to PM_{10} of factors related to secondary particles split by month as a function of the time of the day and day of the week.

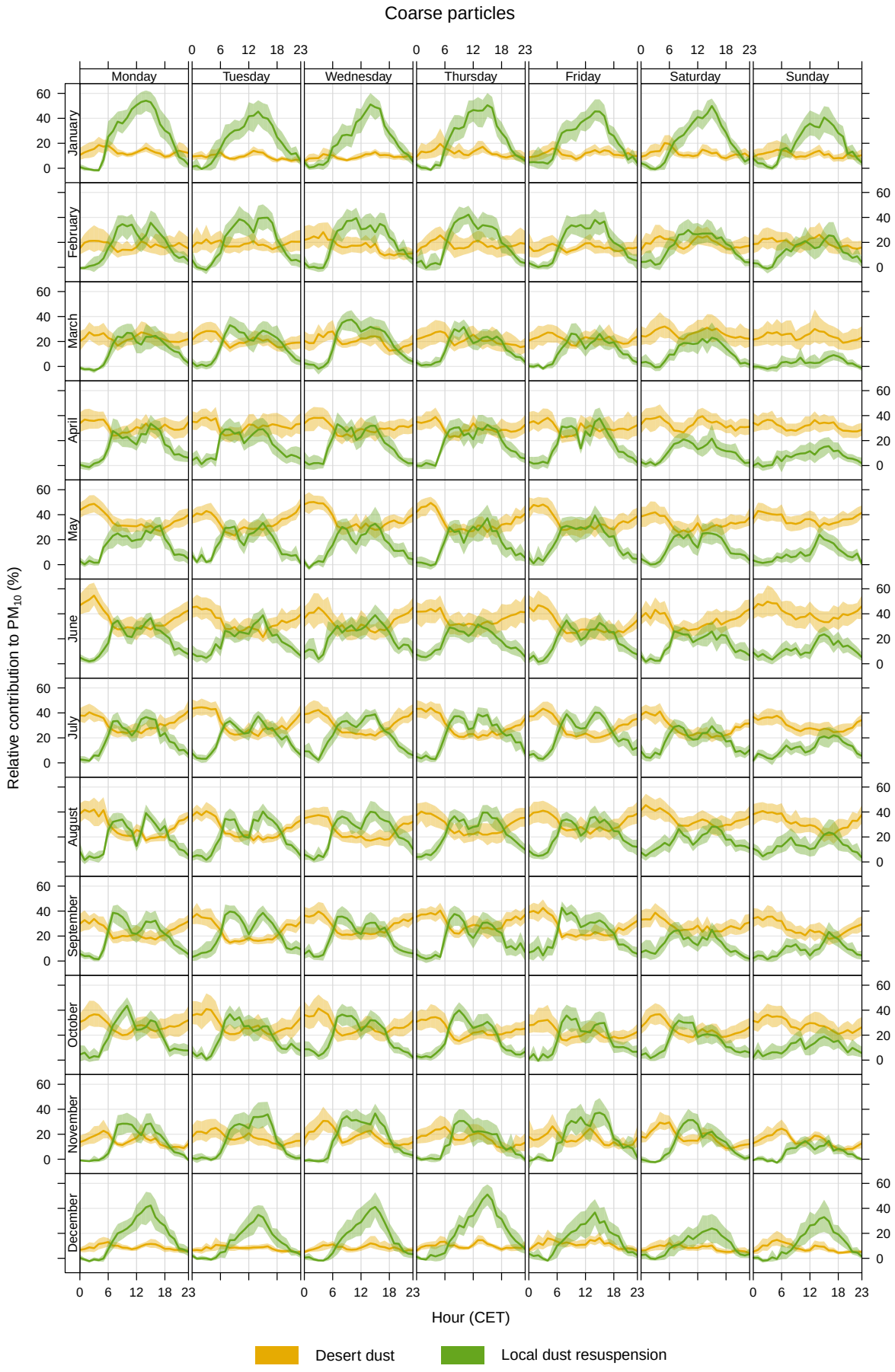

Figure S24: Hourly average percentage contributions to PM_{10} of coarse particles split by month and day of the week.

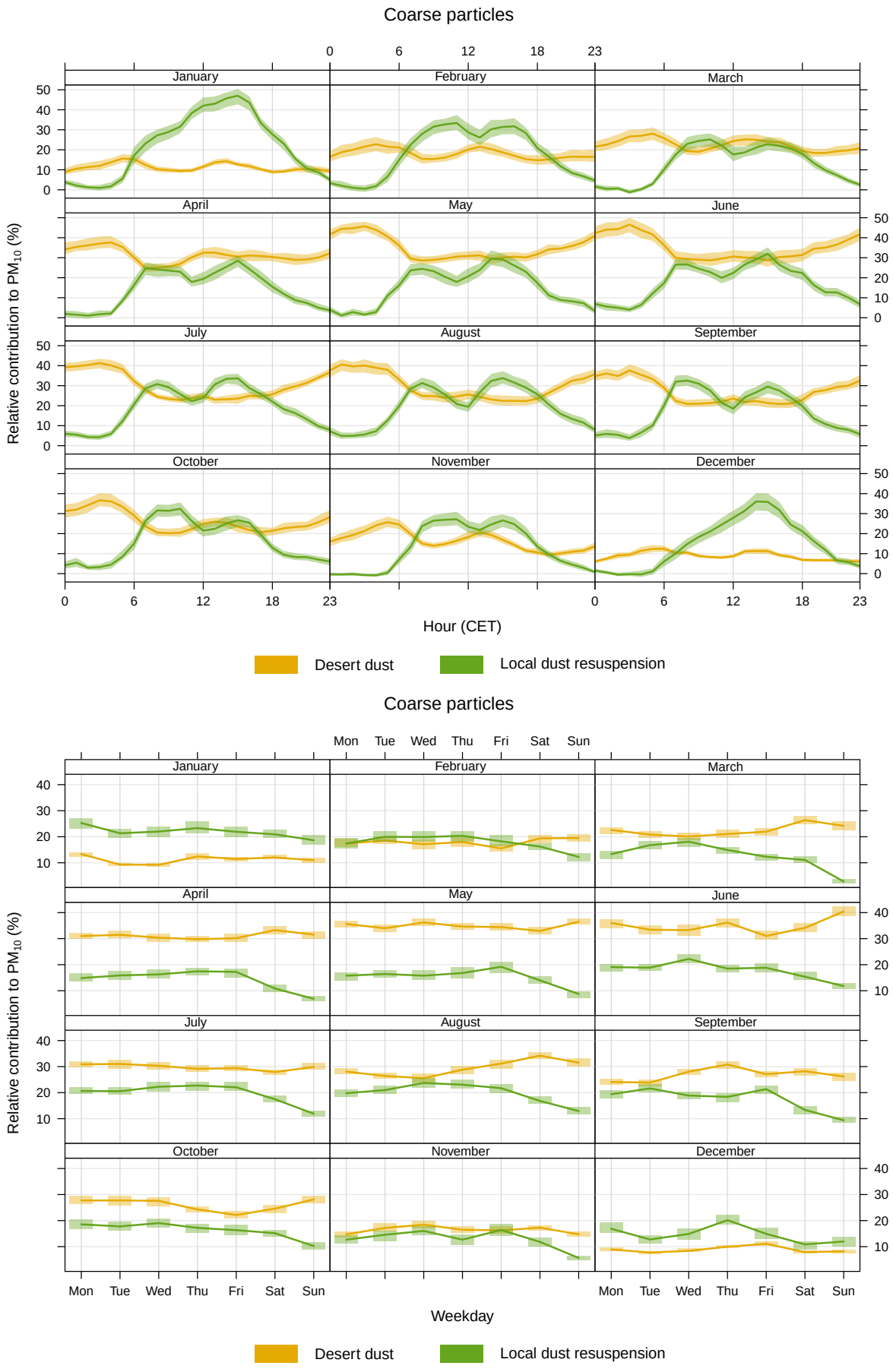

Figure S25: Average percentage contributions to PM_{10} of coarse particles split by month as a function of the time of the day and day of the week.

S13 Dependence on wind

Hourly contributions to PM_{10} from RASPBERRY, unlike daily averages from the chemical PMF, enable correlation with high temporal resolution meteorological data. In this study, we focus on surface wind measurements as they are highly related to PM modulations at the considered site. Ideally, wind data should be obtained from the same location as the aerosol measurements. However, at the Aosta–Downtown station, wind measurements are significantly influenced by the surrounding urban landscape due to the presence of tall buildings. Therefore, for this analysis, wind data from additional stations are used: Aosta–southwest station (approximately 2 km away), Aosta–Saint-Christophe and Aosta–Industrial (on the top of the steel mill). As an example, Fig. S26 presents a conditional probability function (CPF, Ashbaugh et al., 1985) polar plot that combines factor contributions with wind direction and speed measured at the Aosta–southwest station. The colours indicate the ratio of measurements within a wind speed/direction bin when concentrations exceed the 75^{th} percentile to the total number of measurements in that bin. Additionally, Figs. S27–S29 provide similar plots further disaggregated by season, and include wind data from all meteorological stations. It is important to note that, due to a slight change in the orientation of the main valley west of Aosta, northeasterly winds at the Aosta–southwest station correspond to easterly winds at the Aosta–Saint-Christophe station.

The figures generally confirm our earlier source-factor attributions. The highest contributions from traffic emissions at AostaDowntown occur in conjunction with low to moderate wind speeds blowing from the northeastern sector relative to Aosta–southwest (Fig. S26a). Notably, the annual polar plot exhibits a bimodal distribution, with two distinct clusters corresponding to the cold (lower wind speeds) and warm (higher wind speeds) seasons, illustrated more clearly in Figs. S27a–S29a. This pattern likely reflects the local origin of urban traffic emissions during winter, with contributions from the eastern part of the city during the warmer months. The latter may be attributed to higher vehicular density in that area and to traffic-polluted air masses advected from the east, perhaps originating from the eastern side of the region (motorway) or even the Po Basin. The biomass burning factor is associated with calm wind conditions (Fig. S26b), which can be explained by the local origin from the city and its surrounding areas, but also with the generally weak winds prevailing in winter, when biomass burning concentrations peak. Conversely, the condensation mode factor shows its highest contributions in correspondence with stronger easterly winds, which is consistent with the expected contribution of secondary particles transported from the Po Basin (Diémoz et al., 2019). A dependence similar to biomass burning is also observed for the droplet mode factor (Figs. S26d and S27d), which exhibits maximum concentrations during calm conditions with a slight bias towards the eastern sector. However, when wind data from Aosta–Saint-Christophe are used instead of Aosta–southwest, this factor demonstrates a clearer dependence on easterly flows (Fig. S28d), supporting the role of air masses advected from the Po Basin. The polar plot for the dust component (Fig. S26e) reveals a dominance of easterly flows (Fig. S26e). This likely reflects the most frequent surface wind direction during dust events rather than the actual provenance of the air masses, already explored in Sect. 4.2.3 and Fig. 7c. Nevertheless, advection from the Po basin could be partly responsible for transporting 'polluted dust' resulting from entrainment and mixing in the lower atmospheric layers of the Po Valley (crustal elements are present in the sulfate-rich chemical factor, suggesting the potential role of such processes, Figs. S5–S6). Finally, it is noteworthy that local coarse particles (Fig. S26f) are mainly associated with very high wind speeds, originating from both the eastern and western sectors. Unlike other factors, local coarse particles show increased contributions even during westerly flows, including foehn winds typically leading to a drop in the concentrations of most pollutants. This phenomenon occurs due to particle resuspension caused by strong winds, regardless of their provenance direction. Near the city centre, the maximum concentration is found in correspondence to southeasterly winds (Fig. S29f), which may be conducive of coarse particle transport from the steel mill to the Aosta–Downtown station. Indeed, as shown in Fig. S30, the CPF maximum clearly points towards the steel mill. Another probable source in this direction is the large parking lot of the cable car departure, which experiences particular crowding during winter.

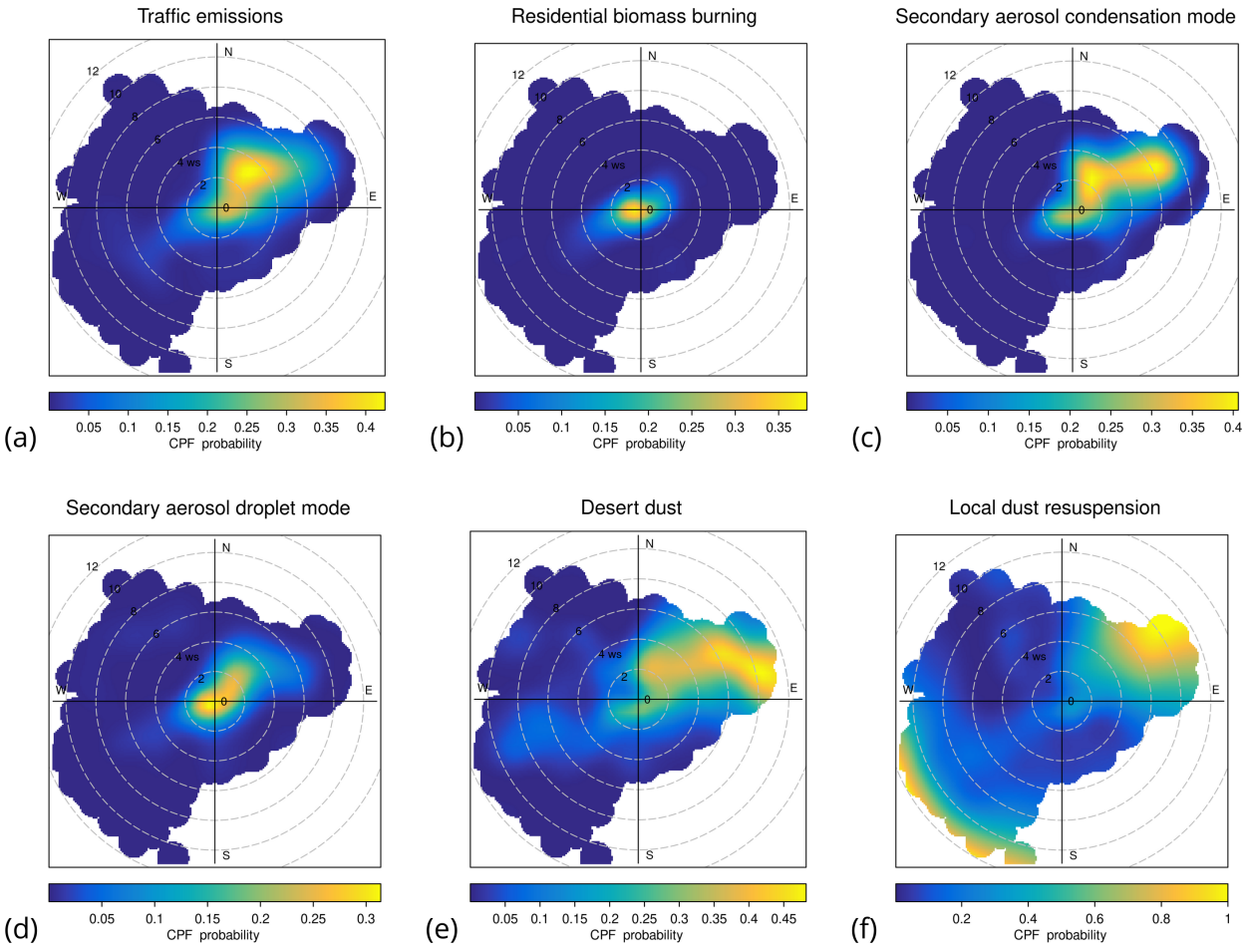

Figure S26: Conditional probability functions for PM_{10} contributions from each factor of RASPBERRY. Data are binned by wind speed (represented as the radial distance from the centre of the plot) and wind direction (polar angle). Colours indicate the ratio of measurements in a bin with concentration exceeding the 75^{th} percentile to the total number of measurements in that bin (Ashbaugh et al., 1985).

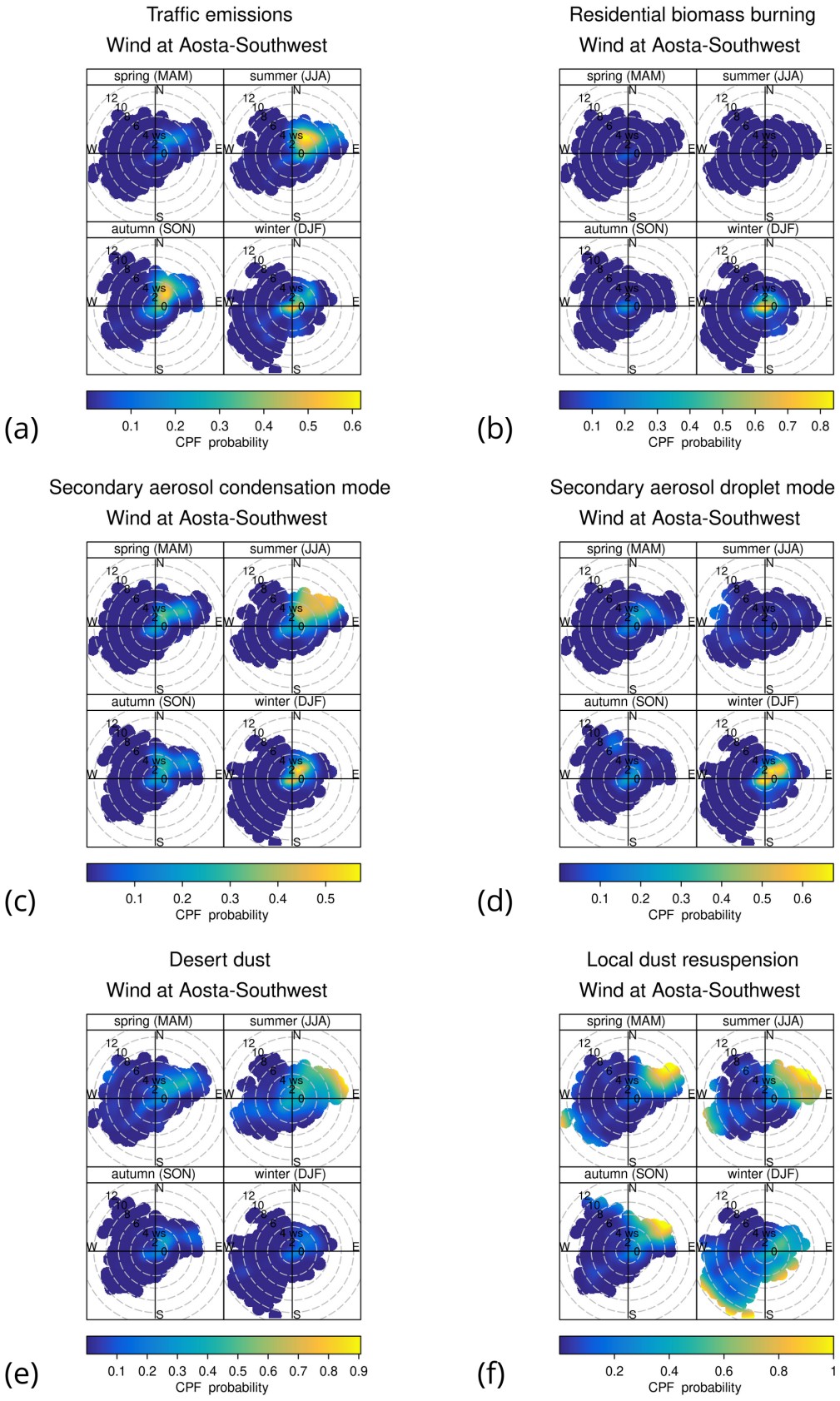

Figure S27: Conditional probability function at the 75$^{\text{th}}$ percentile split by season for all emission factors. Wind is taken from the Aosta–southwest station.

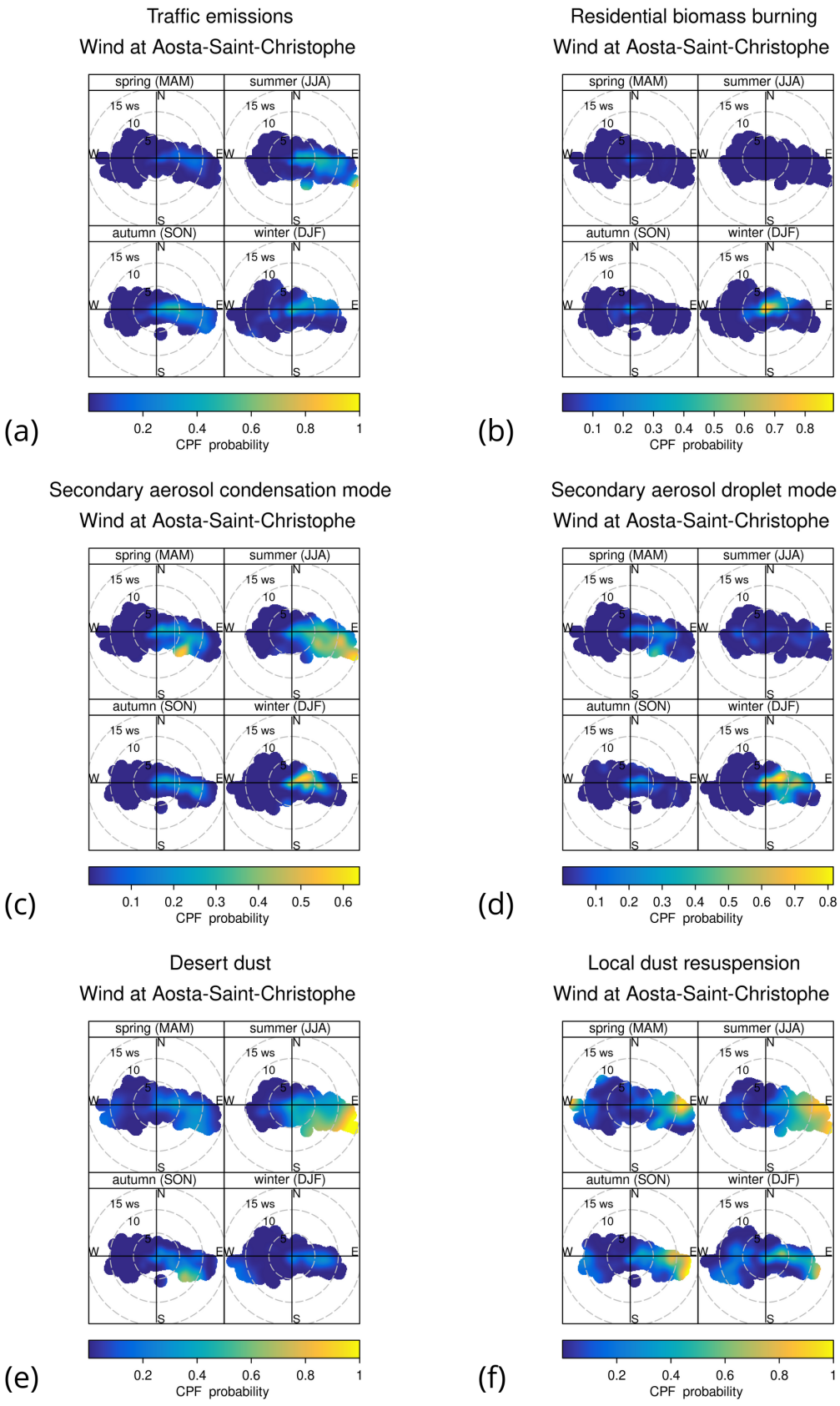

Figure S28: Conditional probability function at the 75$^{\text{th}}$ percentile split by season for all emission factors. Wind is taken from the Aosta–Saint-Christophe station.

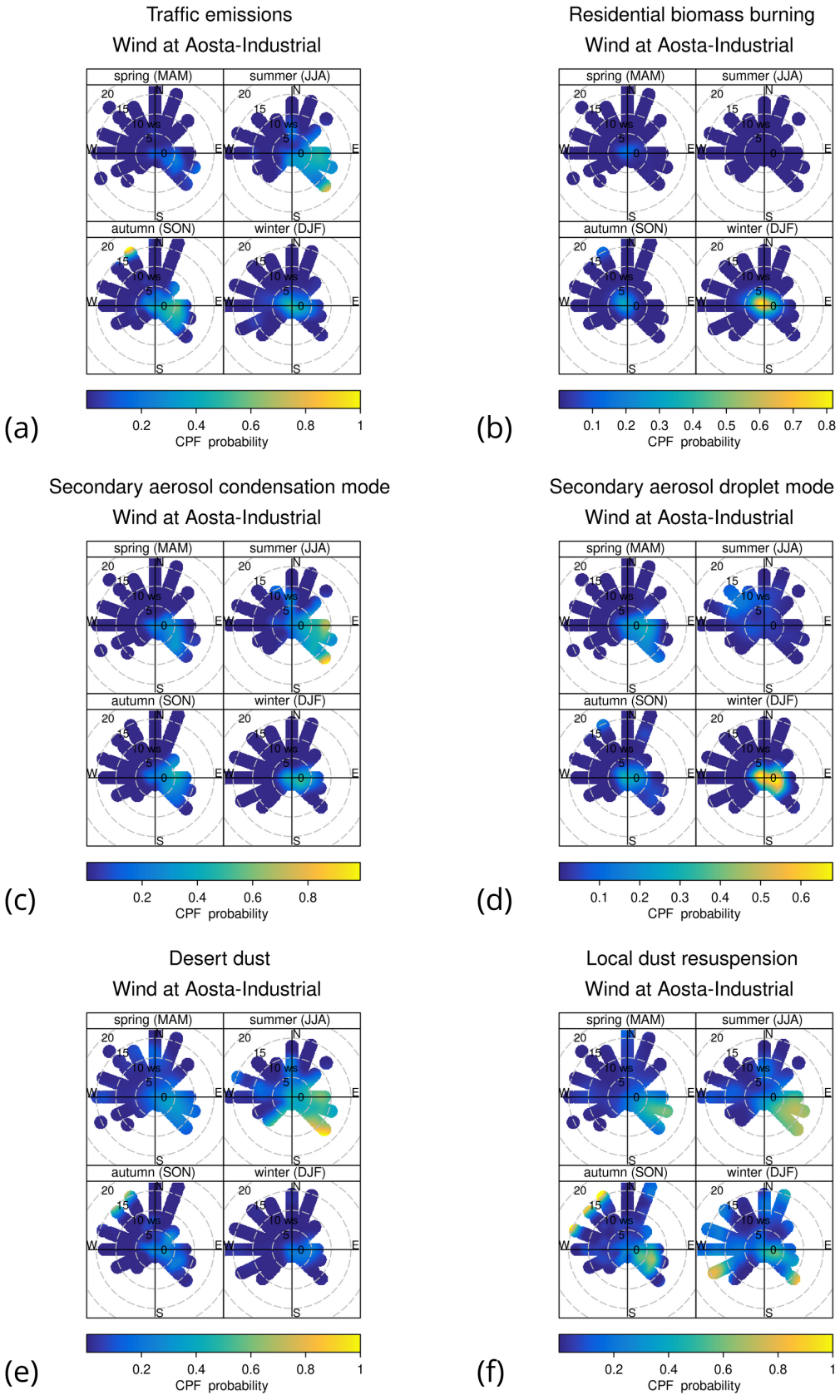

Figure S29: Conditional probability function at the 75$^{\text{th}}$ percentile split by season for all emission factors. Wind is taken from a meteorological station installed on the root of the steel mill. In this case, directions are recorded at discrete angular intervals.

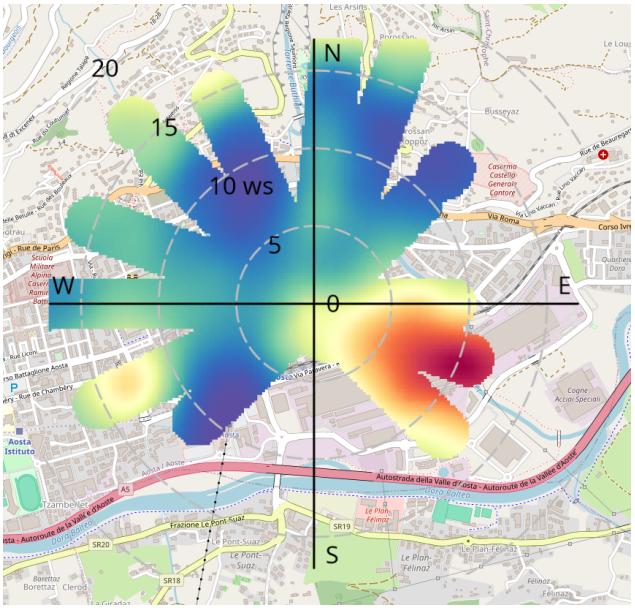

Figure S30: Annual CPF plot for coarse particles and the city map. The highest probability of concentrations exceeding the 75th percentile is associated to southesterly winds.

S14 Comparison of RASPBERRY volume size distributions and previous literature

We examined the available literature reporting in-situ surface measurements of source-resolved PNSDs and PVSDs, including datasets from recent intensive field campaigns where available, in order to compare them with those derived from RASPBERRY and presented in Fig. 3 of the main text. As RASPBERRY identified six factors, these are discussed and compared with available literature data as follows:

1. **Traffic:** As stated in the manuscript, the PVSD exhibits a multimodal structure, indicating contributions from composite sources (Mazzei et al., 2007; Cuccia et al., 2010). A maximum is observed at the lower limit of the diameter range (180 nm), suggesting potentially higher VSD values for smaller particles associated with traffic exhaust (Costabile et al., 2009; El Haddad et al., 2009; Gu et al., 2011; Dall'Osto et al., 2012; Wu et al., 2021), followed by a second mode attributable to resuspension processes. Indeed, Gu et al. (2011), Liu et al. (2014), and Leoni et al. (2018) reported a first PVSD maximum at ∼100–200 nm and a second one at ∼4–5 μm. The latter is consistent with our local PVSD maximum (3.53 μm) above 1 μm, indicating the contribution of non-exhaust emissions. Considering 'fresh traffic' emissions, these can only be approximated by log-normal interpolation of our OPC data (e.g., Ferrero et al., 2011, 2014, 2019). Acknowledging the limitations of such an approach when applied to raw OPC data, the estimated volume mean diameter (VMD) of this factor in RASPBERRY is ∼100 nm, corresponding to a count mean diameter (CMD) of ∼50 nm and a geometric standard deviation (GSD) of 1.61. These values are consistent with the aforementioned studies and support the interpretation of Factor 1.

2. **Residential biomass burning:** The PVSD exhibits a maximum at 305 nm and shows an increasing trend towards the lower limit of the diameter range (180 nm). Gu et al. (2011), Liu et al. (2014), and Leoni et al. (2018) reported PVSD maxima in the ∼100–500 nm range, with CMD values between 40 and 170 nm. Applying log-normal interpolation to our OPC data yields an estimated VMD of ∼230 nm, corresponding to a CMD of ∼170 nm with a GSD of 1.37. These values lie towards the upper end of the reported ranges, however the presence of a local minimum at 264 nm (Fig. 3d) partially affects the log-normal fitting.

3. **Secondary aerosol (condensation mode):** The aforementioned studies by Gu et al. (2011), Liu et al. (2014), and Leoni et al. (2018) reported PVSD peaks at approximately ∼500, ∼250, and ∼300 nm, respectively. The RASPBERRY PVSD associated with this factor is relatively smooth, with an OPC maximum at 264 nm. Log-normal interpolation of the OPC data provides an estimated VMD of ∼240 nm, corresponding to a CMD of ∼220 nm and a GSD of 1.18, in good agreement with previous studies.

4. **Secondary aerosol (droplet mode):** RASPBERRY PVSD exhibits a bimodal structure below 1 μm. The second peak is close to the 'accumulation mode' at ∼400 nm reported by Liu et al. (2014), the 'secondary aerosol' at ∼500 nm described by Gu et al. (2011), and differs from the 'regional pollution' mode at ∼900 nm reported by Leoni et al. (2018). The first peak (∼305 nm) is comparable to the 'aged traffic' mode in Gu et al. (2011) (∼200 nm), the 'secondary ammonium nitrate and sulphate' mode in Liu et al. (2014) (∼250 nm), and the 'urban background' mode in Leoni et al. (2018) (∼250 nm). Overall, this droplet mode appears to represent a complex mixture of urban and regional background aerosols. Log-normal interpolation yields a first VMD of ∼310 nm (CMD ∼270 nm, GSD 1.23) and a second VMD of ∼500 nm (CMD ∼440 nm, GSD 1.22), in good agreement with previous findings.

5. **Desert dust:** RASPBERRY PVSD peaks at 4.072 μm. Log-normal interpolation yields a VMD of ∼3.94 μm, corresponding to a CMD of ∼2.50 μm with a GSD of 1.48. The dust peak reported by Liu et al. (2014) ('fugitive dust', not directly comparable) lies above 1 μm, although the upper size limit prevents identification of the maximum. Gu et al. (2011) reported a peak at ∼3 μm, which is consistent with our findings. It is noted that Leoni et al. (2018) did not identify a desert dust factor.

6. **Local dust resuspension:** RASPBERRY PVSD peaks at 7.782 μm. Log-normal interpolation yields a VMD of ∼5.62 μm, corresponding to a CMD of ∼4.40 μm with a GSD of 1.33. A comparable resuspension peak is not reported by Liu et al. (2014), whereas Gu et al. (2011) identified two volume peaks at ∼300 nm and ∼7 μm, the latter being consistent with our observations. Similarly, the ∼5 μm peak reported by Leoni et al. (2018) for 'industrial coarse particles/road dust' is in agreement with our results.

Based on the above comparison, the robustness of our results is further supported. At the same time, the observed differences highlight the variability of size distribution profiles as a function of location, source characteristics, and sampling period (including interannual variability driven by changes in source features, Kim et al., 2004; Gu et al., 2011; Vu et al., 2015; Leoni et al., 2018; Rivas et al., 2020; Hopke et al., 2022; Harni et al., 2024). This suggests that the profiles presented in Fig. 3 may also serve as a valuable reference for future source apportionment studies and inter-comparisons.

S15 Examples of desert dust layers aloft and entering the mixing layer

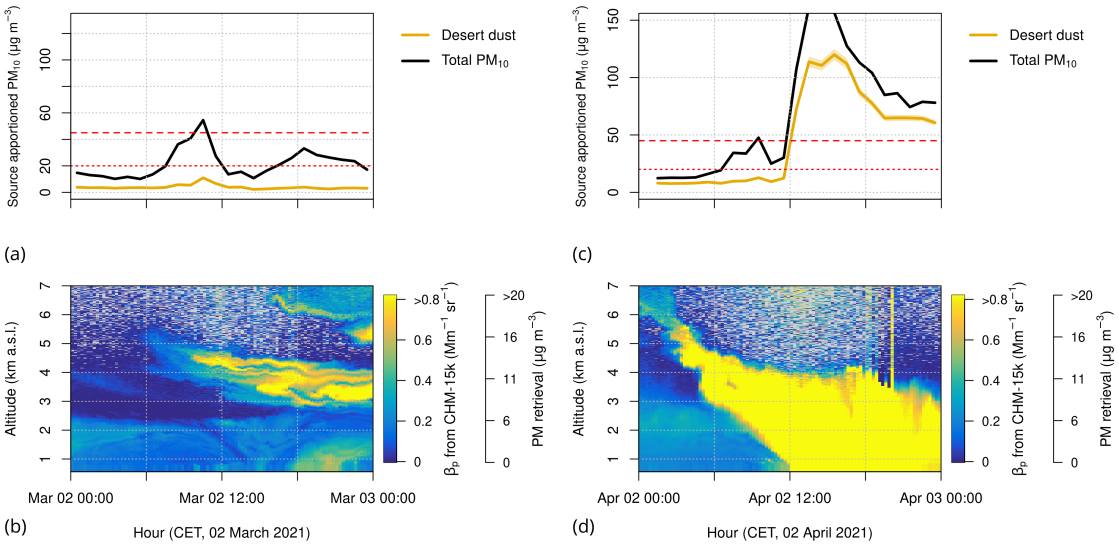

Figure S31: Surface PM attributed to desert dust by RASPBERRY **(a, c)** and ALICENET PM retrievals along the vertical profile **(b, d)**, based on ALC backscatter measurements and the methodology explained by Bellini et al. (2024). Two representative cases of desert dust transport in 2021, selected from those discussed in the main text, are presented: **(a, b)** an elevated layer detected by remote sensing instruments (sun photometer and ALC) throughout the atmospheric column but not observed by surface-level instruments; **(c, d)** a dust layer reaching the surface and significantly affecting local air quality.

S16 HYSPLIT configuration and concentration-weighted trajectories

The HYSPLIT model (Stein et al., 2015; Rolph et al., 2017) is employed to generate 7-day back-trajectories every 6 hours over the entire 2020–2024 period (for a total of more than 7,000 trajectories), based on wind fields from the Global Data Assimilation System (GDAS) at 1° resolution. The trajectory endpoints are set to the coordinates of Aosta at an altitude of 1500 m a.g.l., identified as a representative altitude for both long-range transport and entrainment processes to the surface. For the CWT field calculations, only trajectory points sufficiently close to the surface are considered. Based on the examination of mixing height outputs from the GDAS model and scientific literature (e.g., Barreto et al., 2022), the maximum altitude was set to 2000 m a.g.l. in winter, 4000 m a.g.l. in spring and autumn, and 6000 m a.g.l. in summer.

S17 Coarse particle resuspension and depolarisation ratio from the automated lidar-ceilometer

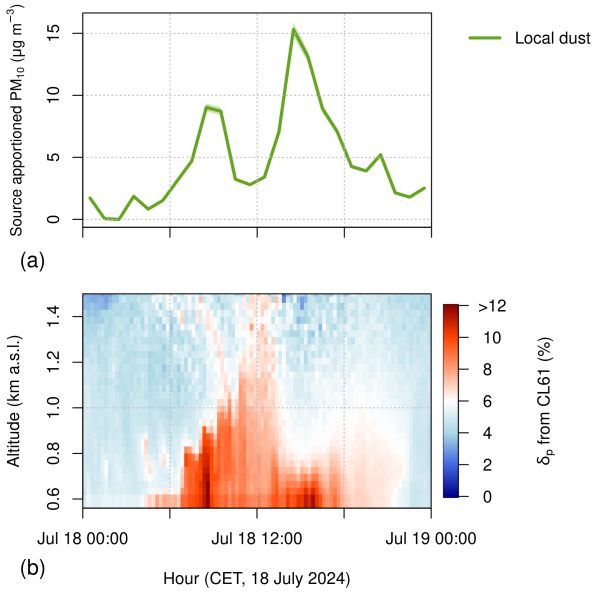

Figure S32: Example of the relationship between **(a)** PM_{10} surface contributions from coarse particles, as derived from RASPBERRY, and **(b)** the evolution of the particle depolarisation vertical profile measured by the CL61 on a typical summer day (18 July 2024). The colour scale limits in the bottom plot have been tweaked to enhance the contrast between conditions of low aerosol backscatter or spherical-shaped particles (low depolarisation) and the presence of irregularly shaped particles in the atmosphere (high depolarisation).

S18 Supporting materials on the comparison between chemical PMF and RASPBERRY

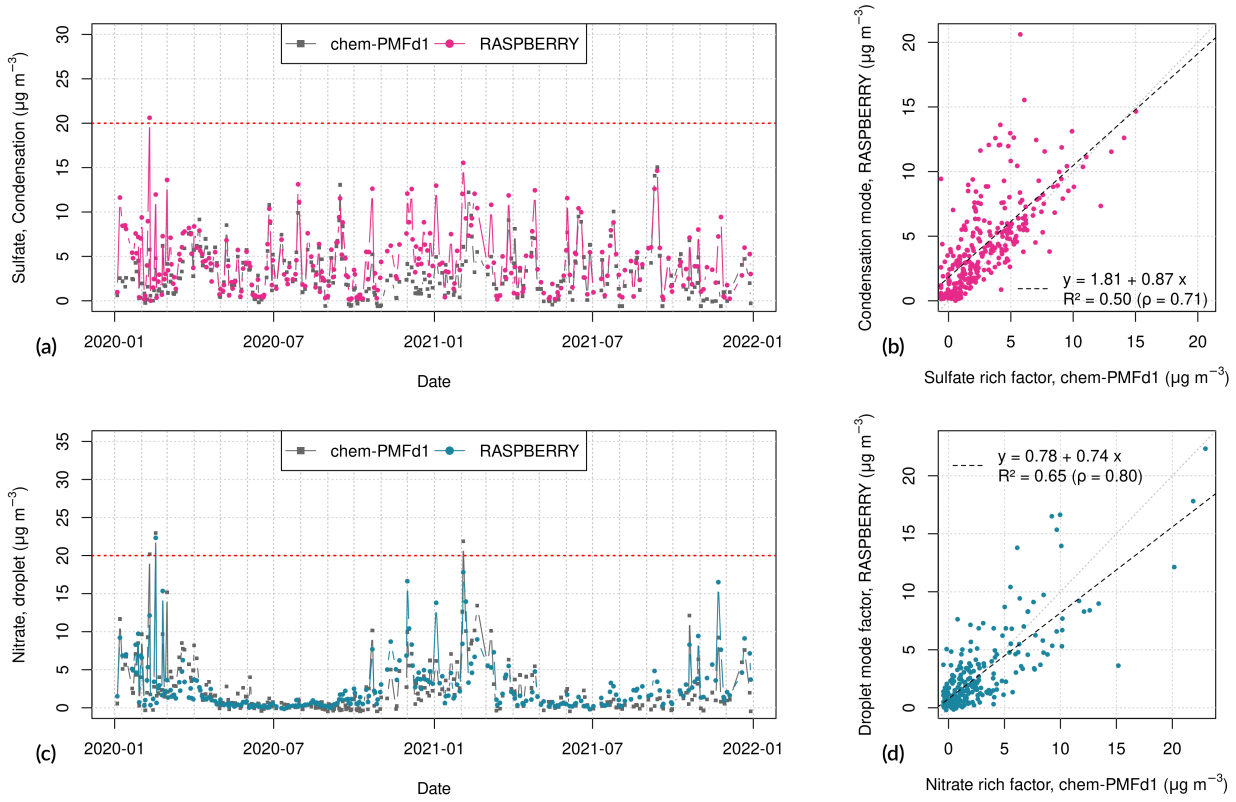

Figure S33: Comparison of PM_{10} source contributions derived from the chemical PMFs (dataset 1, with anion, cation, EC/OC and levoglucosan) and RASPBERRY, presented using time series plots **(a, c)** and scatter plots **(b, d)** with regression equations displayed within the plots. Both plot types include only samples from coincident dates across both datasets, limiting the comparison to the subperiod 2020–2021. Specifically: **(a–b)** represent the contribution from the sulfate-rich factor (chemical PMF) and the condensation mode factor (RASPBERRY); **(c–d)** represent the contribution from the nitrate-rich factor (chemical PMF) and the droplet mode factor (RASPBERRY). Red horizontal line: PM_{10} (annual average) limit value introduced by the 2024/2881/EC AQ directive plotted as reference.

Table S3: Regression coefficients and their standard errors between the PM_{10} contributions from the chemical PMF (x) and RASPBERRY(+EVLS) (y), determined using different regression methods: ordinary least squares (OLS), Deming regression (total least squares, Linnet, 1990), York regression (York et al., 2004), and log-log York regression to account for heteroscedasticity.

Method	Coefficients	Traffic	Biomass burning	Secondary [a]	Coarse [b]
OLS	Slope	0.58 ± 0.04	0.99 ± 0.02	0.99 ± 0.04	0.95 ± 0.03
	Intercept ($\mu g\,m^{-3}$)	0.72 ± 0.06	0.34 ± 0.04	1.62 ± 0.28	1.36 ± 0.19
Deming [c]	Slope	0.60 ± 0.05	1.08 ± 0.04	1.08 ± 0.05	0.96 ± 0.05
	Intercept ($\mu g\,m^{-3}$)	0.70 ± 0.09	0.22 ± 0.03	1.16 ± 0.24	1.31 ± 0.20
York [d]	Slope	1.35 ± 0.12	1.20 ± 0.03	1.32 ± 0.03	1.58 ± 0.03
	Intercept ($\mu g\,m^{-3}$)	-0.16 ± 0.11	0.12 ± 0.01	0.01 ± 0.12	-0.88 ± 0.08
York (log)	Slope	1.05 ± 0.08	0.86 ± 0.02	1.26 ± 0.04	1.32 ± 0.02
	Intercept ($\mu g\,m^{-3}$)	0.01 ± 0.05	0.32 ± 0.02	-0.51 ± 0.08	-0.41 ± 0.03

[a] Sum of sulfate- and nitrate-rich factors from the chemical PMF, and condensation and droplet mode factors from RASPBERRY.
[b] Sum of road salting and crustal factors from the chemical PMF, and desert dust and local dust resuspension from RASPBERRY, excluding data influenced by significant Saharan dust events.
[c] The regression was performed taking into account the actual variance-error ratios obtained from the DISP test of both physical and chemical PMFs. RASPBERRY retrievals were used with this method.
[d] The regression was performed using individual uncertainties calculated through EVLS for both the physical (RASPBERRY+EVLS) and chemical (PMF+EVLS) data sets (Fig. S34). York et al. (2004) regression yields the same coefficients as those obtained using Python's implementation of orthogonal distance regression (ODR).

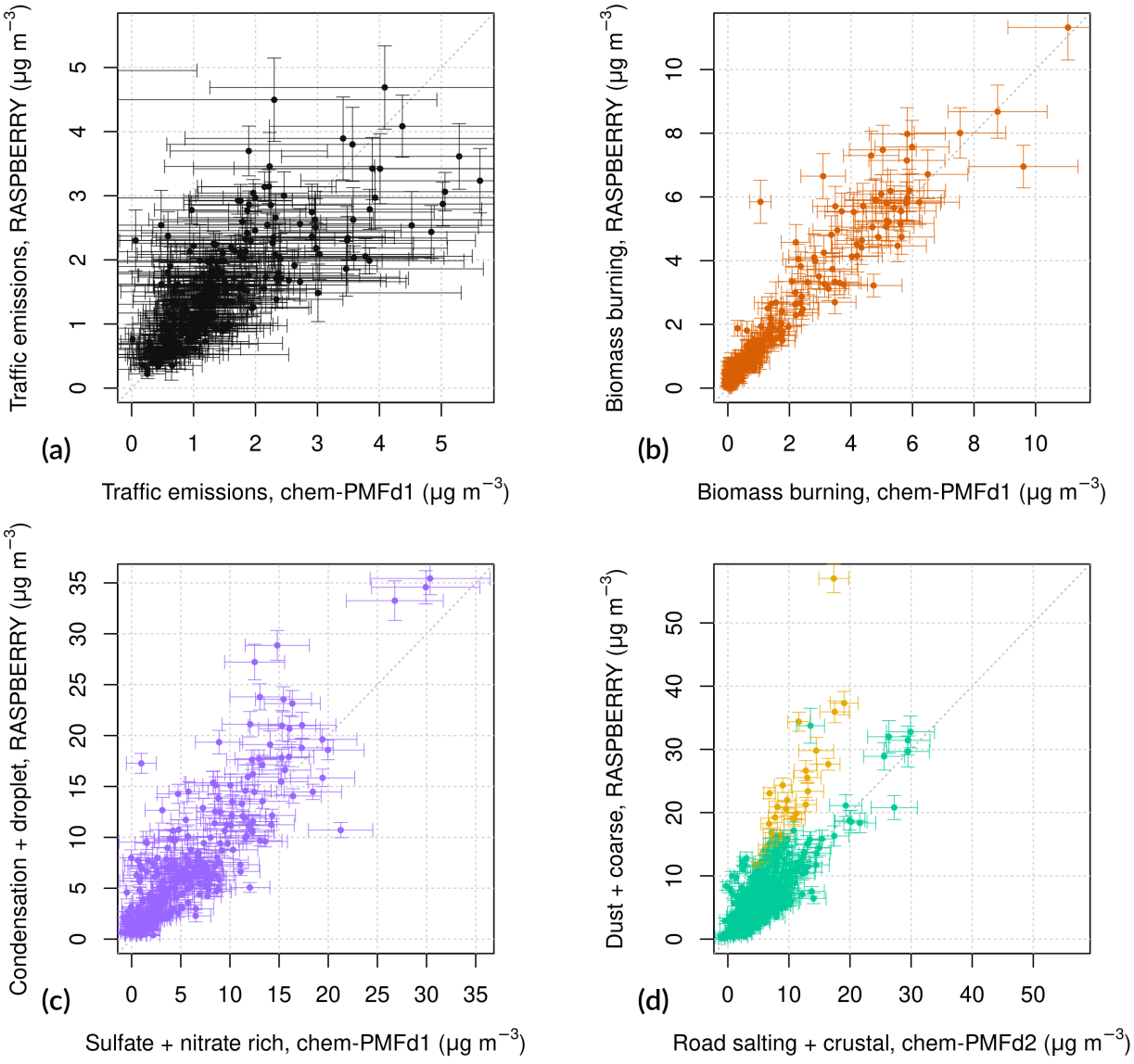

Figure S34: Comparison of daily-averaged PM_{10} source contributions derived from the chemical PMFs (further reprocessed using EVLS) and RASPBERRY+EVLS, shown together with their individual uncertainties. The plots include only samples from coincident dates in both datasets, limiting the comparison to the subperiod 2020–2021. Subfigure **(c)** represents the comparison between the sum of the sulfate- and nitrate-rich factors from the chemical PMF and the sum of the condensation- and droplet-mode factors from RASPBERRY+EVLS. Subfigure **(d)** illustrates the comparison between the sum of the road-salting and crustal factors from the chemical PMF (dataset 2) and the sum of desert dust and local dust resuspension from RASPBERRY+EVLS. Data influenced by significant Saharan dust events are shown in yellow in subfigure **(d)**.

S19 Case study: traffic exhaust and non-exhaust during winter holidays 2024

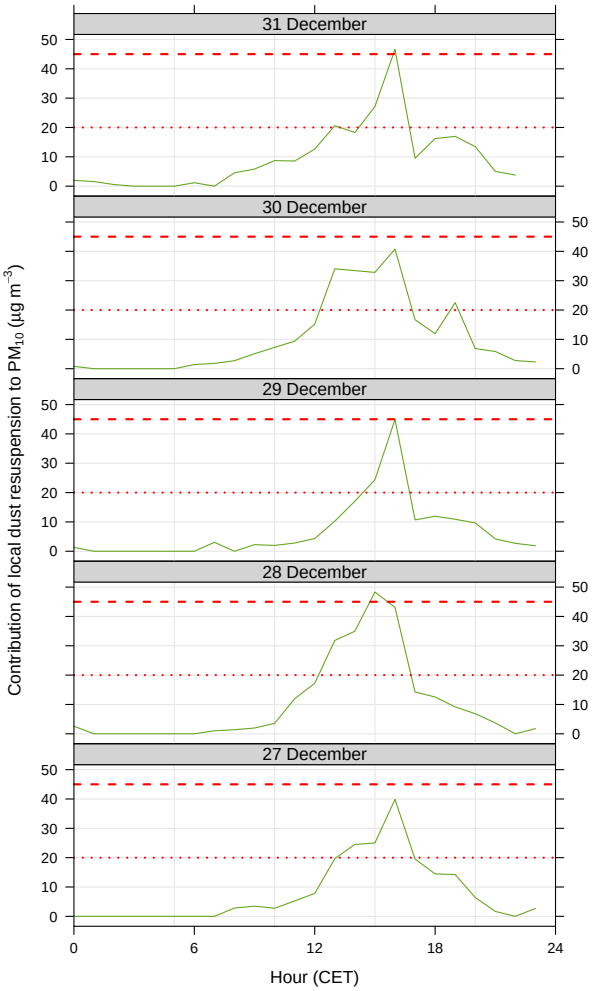

Figure S35: Contribution of local dust resuspension to PM_{10} in Aosta–Downtown, as determined from RASPBERRY, in the period 27–31 December 2024. Red horizontal lines: PM_{10} annual and daily average limit values introduced by the 2024/2881/EC AQ directive.

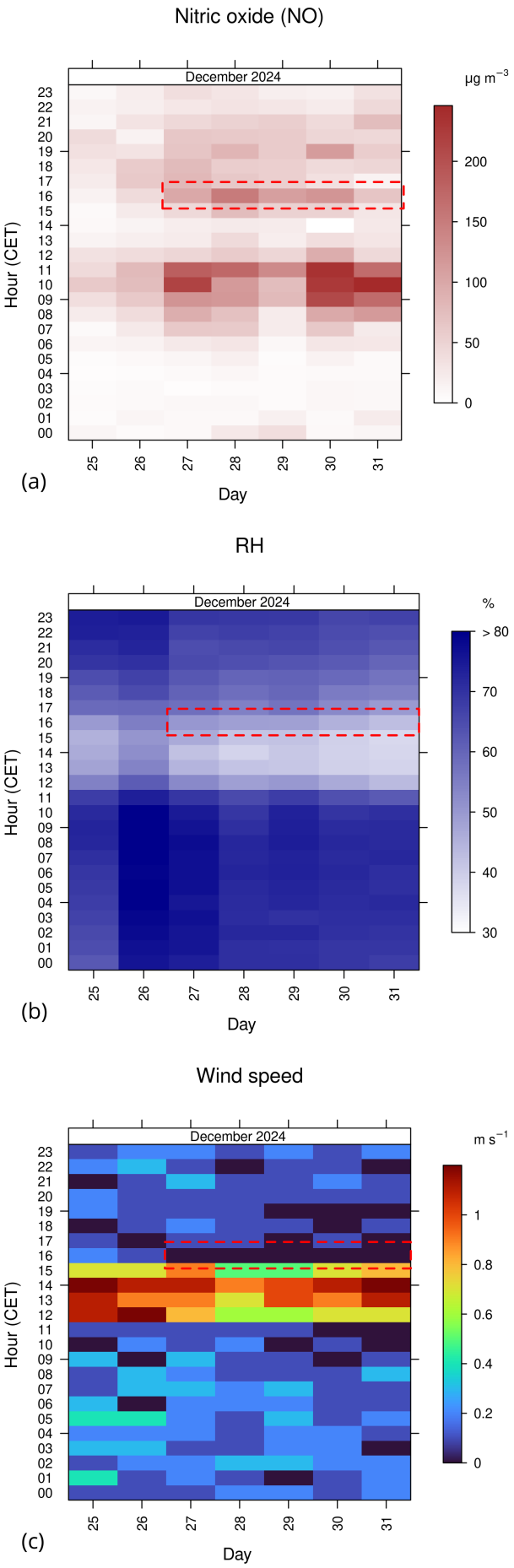

Figure S36: Day/hour diagrams depicting **(a)** nitric oxide concentrations, **(b)** relative humidity, and **(c)** wind speed from 25 to 31 December 2024. The period of peak coarse particle concentrations in the afternoon is highlighted with a dashed contour.

S20 Case study: summertime advection of secondary particles

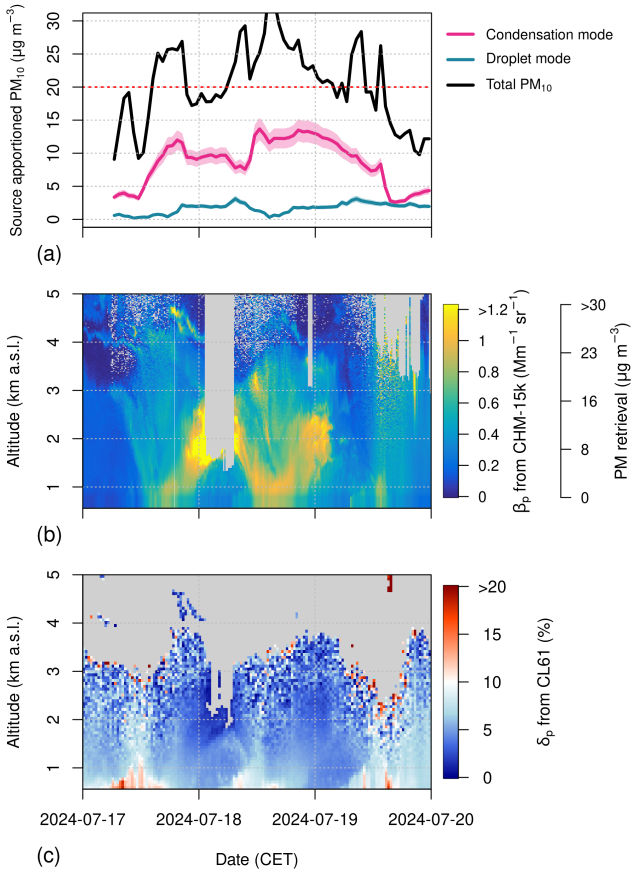

Figure S37: Transport episode of secondary-rich particles in July 2024. **(a)** PM_{10} contributions from the condensation and droplet mode factors, derived through the physical source apportionment. Red horizontal line: PM_{10} (annual average) limit value introduced by the 2024/2881/EC AQ directive plotted as reference. **(b)** Vertical profile of ALICENET PM retrievals based on CHM-15k ALC particle backscatter measurements, showing the arrival of an aerosol-rich air mass on the afternoon of 17 July 2024, the formation of a residual layer overnight, and its subsequent entrainment, likely reinforced by additional advection, over the course of the following day. **(c)** Particle depolarisation ratio from the CL61 ALC.

S21 Case study: smoke transport from Canada in 2024

During the event, analysed here from 20 to 24 August 2024, the AOD at 500 nm measured by the sun photometer increases to 0.3–0.4. Larger AOD values are observed in the morning, with sharp decreases during the day, possibly indicating the presence of hygroscopic material. The extinction Ångström exponent remains about 1.3–1.5 throughout the event. The single scattering albedo consistently stays at 0.9 and above. The size distribution shows a maximum between 0.2 and 0.3 ţm radius.

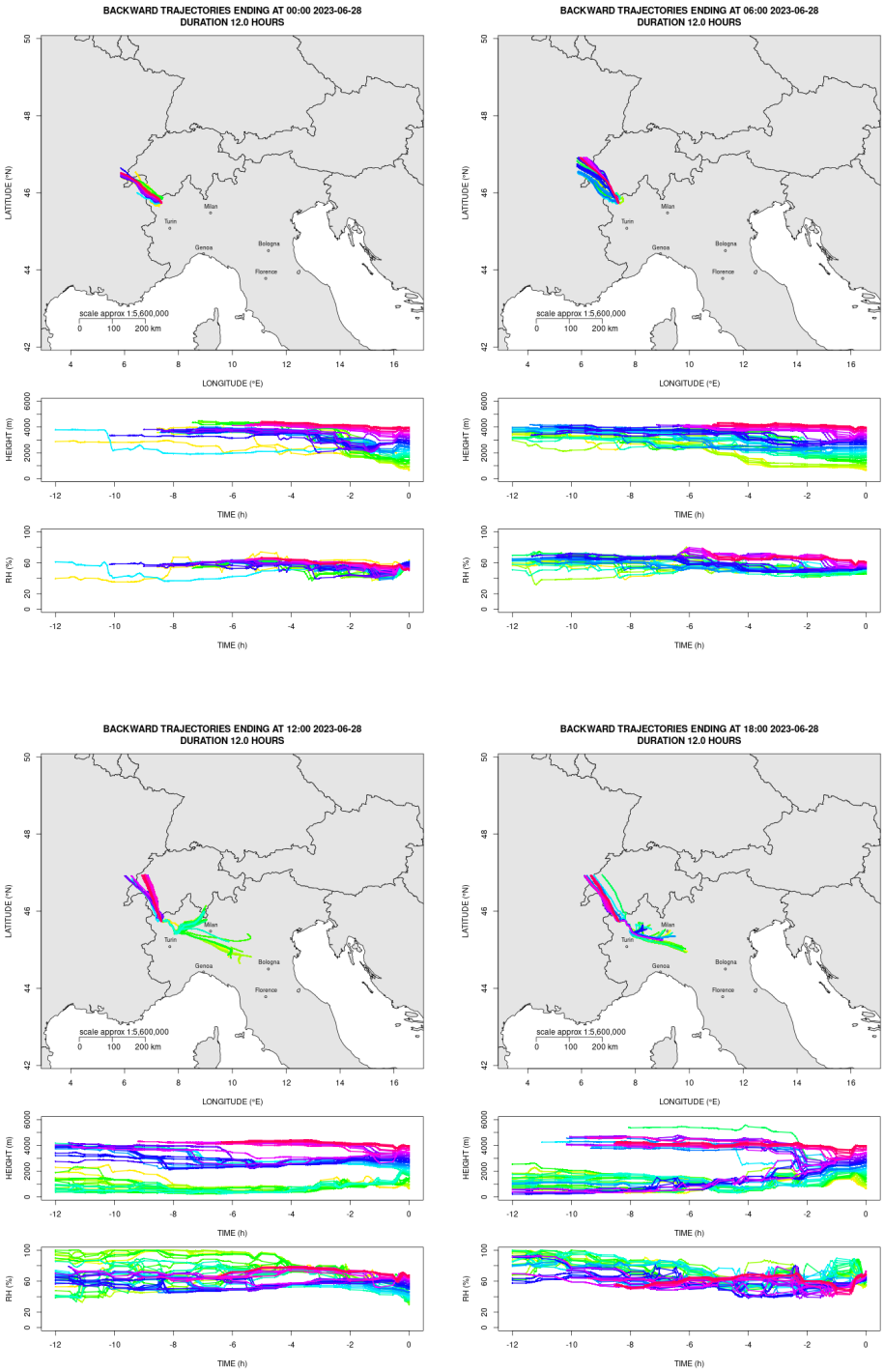

Figure S38: Back-trajectories obtained using the Consortium for Small-scale Modelling (COSMO) model on 28 June 2023, at 6-hour intervals from midnight (see Diémoz et al. (2019) for details of the calculations). The altitude of the back-trajectories and the relative humidity of the corresponding air masses are also displayed. The trajectories are truncated northwest of the Aosta Valley due to the domain boundary of the Italian COSMO model variant.

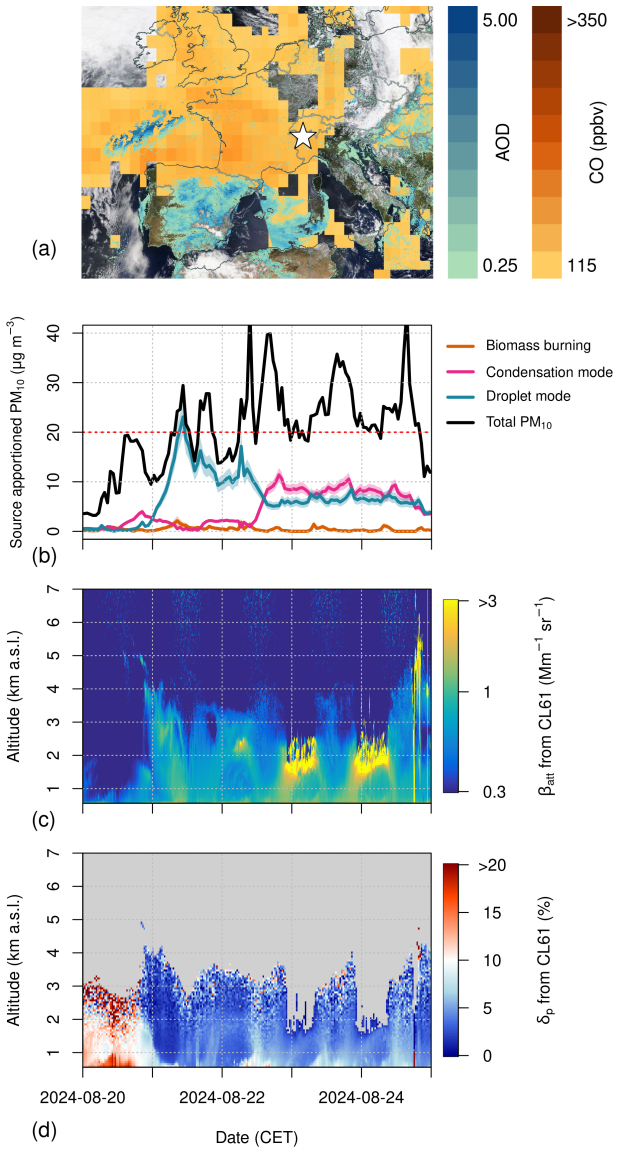

Figure S39: Transport of smoke from Canada to Europe in August 2024. **(a)** Satellite image (21 August 2024) with a MODIS/Terra corrected reflectance background. Aosta is indicated by a star marker. Aerosol Optical Depth (AOD) at 470 nm, retrieved from the MODIS spectroradiometer onboard the Terra and Aqua satellites (MAIAC algorithm, v6.1 STD, 1-km resolution), and carbon monoxide concentrations at 500 hPa from nighttime AIRS/Aqua measurements (v6 STD, L3) are superimposed using two different colour scales (source: `worldview.earthdata.nasa.gov`). **(b)** PM_{10} contributions from the condensation and droplet modes, derived from RASPBERRY. Red horizontal line: PM_{10} (annual average) limit value introduced by the 2024/2881/EC AQ directive plotted as reference. **(c)** Vertical profiles of attenuated backscatter from the CL61 ALC. Notice the logarithmic colour scale. The CHM-15k ALC was temporarily installed at another station and ALICENET PM inversions from CL61 are not yet supported. **(d)** Particle depolarisation ratio from the CL61 ALC.

References

Allen, G. A., Miller, P. J., Rector, L. J., Brauer, M., and Su, J. G.: Characterization of Valley Winter Woodsmoke Concentrations in Northern NY Using Highly Time-Resolved Measurements, Aerosol and Air Qual. Res., 11, 519530, https://doi.org/10.4209/aaqr.2011.03.0031, 2011.

Ashbaugh, L. L., Malm, W. C., and Sadeh, W. Z.: A residence time probability analysis of sulfur concentrations at grand Canyon National Park, Atmos. Environ., 19, 1263–1270, https://doi.org/10.1016/0004-6981(85)90256-2, 1985.

Aujay-Plouzeau, R.: Guide méthodologique pour la mesure du ńBlack Carbonż par Aethalomètre multi longueur d'onde AE33 dans l'air ambiant (Version 2020), Tech. rep., Ineris, `https://www.lcsqa.org/system/files/media/documents/LCSQA2019-Guide_mesure_BlackCarbon_par_AE33_VF03-Approuv%C3%A9CPS15122020.pdf`, 2020.

Barreto, A., Cuevas, E., García, R. D., Carrillo, J., Prospero, J. M., Ilić, L., Basart, S., Berjón, A. J., Marrero, C. L., Hernández, Y., Bustos, J. J., Ničković, S., and Yela, M.: Long-term characterisation of the vertical structure of the Saharan Air Layer over the Canary Islands using lidar and radiosonde profiles: implications for radiative and cloud processes over the subtropical Atlantic Ocean, Atmos. Chem. Phys., 22, 739–763, https://doi.org/10.5194/acp-22-739-2022, 2022.

Bellini, A., Diémoz, H., Di Liberto, L., Gobbi, G. P., Bracci, A., Pasqualini, F., and Barnaba, F.: ALICENET – an Italian network of automated lidar ceilometers for four-dimensional aerosol monitoring: infrastructure, data processing, and applications, Atmos. Meas. Tech., 17, 6119–6144, https://doi.org/10.5194/amt-17-6119-2024, 2024.

Bernardoni, V., Pileci, R. E., Caponi, L., and Massabò, D.: The Multi-Wavelength Absorption Analyzer (MWAA) Model as a Tool for Source and Component Apportionment Based on Aerosol Absorption Properties: Application to Samples Collected in Different Environments, Atmosphere, 8, https://doi.org/10.3390/atmos8110218, 2017.

Bhandari, S., Arub, Z., Habib, G., Apte, J. S., and Hildebrandt Ruiz, L.: Source apportionment resolved by time of day for improved deconvolution of primary source contributions to air pollution, Atmos. Meas. Tech., 15, 6051–6074, https://doi.org/10.5194/amt-15-6051-2022, 2022.

Chen, J., Dai, Q., Zhang, X., Tian, Y., Feng, Y., and Hopke, P. K.: PMF Source Contribution Uncertainty Estimation via Effective Variance Least Squares, ACS ES&T Air, 2, 3045–3053, https://doi.org/10.1021/acsestair.5c00312, 2025.

Chien, C.-H., Theodore, A., Wu, C.-Y., Hsu, Y.-M., and Birky, B.: Upon correlating diameters measured by optical particle counters and aerodynamic particle sizers, J. Aerosol Sci., 101, 77–85, https://doi.org/10.1016/j.jaerosci.2016.05.011, 2016.

Costabile, F., Birmili, W., Klose, S., Tuch, T., Wehner, B., Wiedensohler, A., Franck, U., König, K., and Sonntag, A.: Spatio-temporal variability and principal components of the particle number size distribution in an urban atmosphere, Atmos. Chem. Phys., 9, 3163–3195, https://doi.org/10.5194/acp-9-3163-2009, 2009.

Cuccia, E., Bernardoni, V., Massabò, D., Prati, P., Valli, G., and Vecchi, R.: An alternative way to determine the size distribution of airborne particulate matter, Atmos. Environ., 44, 3304–3313, https://doi.org/10.1016/j.atmosenv.2010.05.045, 2010.

Dai, Q. and Hopke, P. K.: R code for EVLS-CMB source apportionment, https://doi.org/10.5281/zenodo.17767035, 2025.

Dall'Osto, M., Beddows, D. C. S., Pey, J., Rodriguez, S., Alastuey, A., Harrison, R. M., and Querol, X.: Urban aerosol size distributions over the Mediterranean city of Barcelona, NE Spain, Atmos. Chem. Phys., 12, 10 693–10 707, https://doi.org/10.5194/acp-12-10693-2012, 2012.

Diémoz, H., Gobbi, G. P., Magri, T., Pession, G., Pittavino, S., Tombolato, I. K. F., Campanelli, M., and Barnaba, F.: Transport of Po Valley aerosol pollution to the northwestern Alps – Part 2: Long-term impact on air quality, Atmos. Chem. Phys., 19, 10 129–10 160, https://doi.org/10.5194/acp-19-10129-2019, 2019.

Diémoz, H., Tombolato, I. K. F., Zublena, M., Magri, T., and Ferrero, L.: The impact of biomass burning emissions on PM concentration in the Greater Alpine region, in: Proceedings of 12th International Conference on Air Quality, Science and Application, p. 26, Hatfield, UK, 10.18745/pb.22217, 2020.

Diémoz, H., Magri, T., Pession, G., Tarricone, C., Tombolato, I. K. F., Fasano, G., and Zublena, M.: Air Quality in the Italian Northwestern Alps during Year 2020: Assessment of the COVID-19 ńLockdown Effectż from Multi-Technique Observations and Models, Atmosphere, 12, https://doi.org/10.3390/atmos12081006, 2021.

El Haddad, I., Marchand, N., Dron, J., Temime-Roussel, B., Quivet, E., Wortham, H., Jaffrezo, J. L., Baduel, C., Voisin, D., Besombes, J. L., and Gille, G.: Comprehensive primary particulate organic characterization of vehicular exhaust emissions in France, Atmos. Environ., 43, 6190–6198, https://doi.org/10.1016/j.atmosenv.2009.09.001, 2009.

European Commission: Directive 2008/50/EC of the European Parliament and of the Council on ambient air quality and cleaner air for Europe, in: 2008/50/EC, edited by European Parliament, 2008.

Ferrero, L., Mocnik, G., Ferrini, B., Perrone, M., Sangiorgi, G., and Bolzacchini, E.: Vertical profiles of aerosol absorption coefficient from micro-Aethalometer data and Mie calculation over Milan, Sci. Total Environ., 409, 2824–2837, https://doi.org/10.1016/j.scitotenv.2011.04.022, 2011.

Ferrero, L., Castelli, M., Ferrini, B. S., Moscatelli, M., Perrone, M. G., Sangiorgi, G., D'Angelo, L., Rovelli, G., Moroni, B., Scardazza, F., Močnik, G., Bolzacchini, E., Petitta, M., and Cappelletti, D.: Impact of black carbon aerosol over Italian basin valleys: high-resolution measurements along vertical profiles, radiative forcing and heating rate, Atmos. Chem. Phys., 14, 9641–9664, https://doi.org/10.5194/acp-14-9641-2014, 2014.

Ferrero, L., Ritter, C., Cappelletti, D., Moroni, B., Monik, G., Mazzola, M., Lupi, A., Becagli, S., Traversi, R., Cataldi, M., Neuber, R., Vitale, V., and Bolzacchini, E.: Aerosol optical properties in the Arctic: The role of aerosol chemistry and dust composition in a closure experiment between Lidar and tethered balloon vertical profiles, Sci. Total Environ., 686, 452–467, https://doi.org/10.1016/j.scitotenv.2019.05.399, 2019.

Ferrero, L., Losi, N., Rigler, M., Gregori, A., Colombi, C., D'Angelo, L., Cuccia, E., Cefalì, A., Gini, I., Doldi, A., Cerri, S., Maroni, P., Cipriano, D., Markuszewski, P., and Bolzacchini, E.: Determining the Aethalometer multiple scattering enhancement factor C from the filter loading parameter, Sci. Total Environ., 917, 170 221, https://doi.org/10.1016/j.scitotenv.2024.170221, 2024.

Forello, A. C., Bernardoni, V., Calzolai, G., Lucarelli, F., Massabò, D., Nava, S., Pileci, R. E., Prati, P., Valentini, S., Valli, G., and Vecchi, R.: Exploiting multi-wavelength aerosol absorption coefficients in a multi-time resolution source apportionment study to retrieve source-dependent absorption parameters, Atmos. Chem. Phys., 19, 11 235–11 252, https://doi.org/10.5194/acp-19-11235-2019, 2019.

Forello, A. C., Cunha-Lopes, I., Almeida, S. M., Alves, C. A., Tchepel, O., Crova, F., and Vecchi, R.: Insights on the combination of off-line and on-line measurement approaches for source apportionment studies, Sci. Total Environ., 900, 165 860, https://doi.org/10.1016/j.scitotenv.2023.165860, 2023.

Grange, S. K., Lötscher, H., Fischer, A., Emmenegger, L., and Hueglin, C.: Evaluation of equivalent black carbon source apportionment using observations from Switzerland between 2008 and 2018, Atmos. Meas. Tech., 13, 1867–1885, https://doi.org/10.5194/amt-13-1867-2020, 2020.

Gu, J., Pitz, M., Schnelle-Kreis, J., Diemer, J., Reller, A., Zimmermann, R., Soentgen, J., Stoelzel, M., Wichmann, H.-E., Peters, A., and Cyrys, J.: Source apportionment of ambient particles: Comparison

of positive matrix factorization analysis applied to particle size distribution and chemical composition data, Atmos. Environ., 45, 1849–1857, https://doi.org/10.1016/j.atmosenv.2011.01.009, 2011.

Harni, S. D., Aurela, M., Saarikoski, S., Niemi, J. V., Portin, H., Manninen, H., Leinonen, V., Aalto, P., Hopke, P. K., Petäjä, T., Rönkkö, T., and Timonen, H.: Source apportionment of particle number size distribution at the street canyon and urban background sites, Atmos. Chem. Phys., 24, 12 143–12 160, https://doi.org/10.5194/acp-24-12143-2024, 2024.

Hasheminassab, S., Pakbin, P., Delfino, R. J., Schauer, J. J., and Sioutas, C.: Diurnal and seasonal trends in the apparent density of ambient fine and coarse particles in Los Angeles, Environ. Pollut., 187, 1–9, https://doi.org/10.1016/j.envpol.2013.12.015, 2014.

Hayfield, T. and Racine, J. S.: Nonparametric Econometrics: The np Package, J. Stat. Softw., 27, 1–32, https://doi.org/10.18637/jss.v027.i05, 2008.

Hopke, P. K., Feng, Y., and Dai, Q.: Source apportionment of particle number concentrations: A global review, Sci. Total Environ., 819, 153 104, https://doi.org/10.1016/j.scitotenv.2022.153104, 2022.

Kim, E., Hopke, P. K., Larson, T. V., and Covert, D. S.: Analysis of Ambient Particle Size Distributions Using Unmix and Positive Matrix Factorization, Environ. Sci. Tech., 38, 202–209, https://doi.org/10.1021/es030310s, 2004.

Leoni, C., Pokorná, P., Hovorka, J., Masiol, M., Topinka, J., Zhao, Y., Kmal, K., Cliff, S., Mikuka, P., and Hopke, P. K.: Source apportionment of aerosol particles at a European air pollution hot spot using particle number size distributions and chemical composition, Environ. Pollut., 234, 145–154, https://doi.org/10.1016/j.envpol.2017.10.097, 2018.

Linnet, K.: Estimation of the linear relationship between the measurements of two methods with proportional errors, Stat. Med., 9, 1463–1473, https://doi.org/10.1002/sim.4780091210, 1990.

Liu, Z., Hu, B., Liu, Q., Sun, Y., and Wang, Y.: Source apportionment of urban fine particle number concentration during summertime in Beijing, Atmos. Environ., 96, 359–369, https://doi.org/10.1016/j.atmosenv.2014.06.055, 2014.

Marsteen, L. and Hak, C.: NILU Report 21/2021: PM10/PM2.5 comparison exercise in Oslo, Norway. Study in 2015–2016 and 2018, Tech. rep., Norwegian Institute for Air Research (NILU), ISBN 978-82-425-3059-2, ISSN 2464-3327, 2021.

Mazzei, F., Lucarelli, F., Nava, S., Prati, P., Valli, G., and Vecchi, R.: A new methodological approach: The combined use of two-stage streaker samplers and optical particle counters for the characterization of airborne particulate matter, Atmos. Environ., 41, 5525–5535, https://doi.org/10.1016/j.atmosenv.2007.04.012, 2007.

Norris, G., Duvall, R., and Brown, S.: EPA Positive Matrix Factorization (PMF) 5.0 Fundamentals and User Guide, U.S. Environmental Protection Agency Office of Research and Development Washington, DC 20460, `https://www.epa.gov/sites/default/files/2015-02/documents/pmf_5.0_user_guide.pdf`, ePA/600/R-14/108, 2014.

Ogulei, D., Hopke, P. K., Zhou, L., Pancras, J. P., Nair, N., and Ondov, J. M.: Source apportionment of Baltimore aerosol from combined size distribution and chemical composition data, Atmos. Environ., 40, 396–410, https://doi.org/10.1016/j.atmosenv.2005.11.075, 2006.

Ogulei, D., Hopke, P. K., Chalupa, D. C., , and Utell, M. J.: Modeling Source Contributions to Submicron Particle Number Concentrations Measured in Rochester, New York, Aerosol Sci. Tech., 41, 179–201, https://doi.org/10.1080/02786820601116012, 2007.

Pakkanen, T. A., Kerminen, V.-M., Korhonen, C. H., Hillamo, R., Aarnio, P., Koskentalo, T., and Maenhaut, W.: Use of atmospheric elemental size distributions in estimating aerosol sources in the Helsinki area, Atmos. Environ., 35, 5537–5551, https://doi.org/10.1016/S1352-2310(01)00232-1, 2001.

PALAS GmbH: Report on supplementary testing of the Fidaső 200 S respectively Fidaső 200 measuring system manufactured by PALAS GmbH for the components suspended particulate matter PM10 and PM2.5, TÜV-report: 936/21227195/C, chap. Operating Manual Fine Dust Monitor System Fidaső - Version V0230816, TÜV Rheinland Energie und Umwelt GmbH, https://www.palas.de/file/ea8697/application/octet-stream/Palas+T%C3%9CV+Fidas+System, 2016.

Patton, A., Politis, D. N., and White, H.: Correction to "Automatic Block-Length Selection for the Dependent Bootstrap" by D. Politis and H. White, Economet. Rev., 28, 372–375, https://doi.org/10.1080/07474930802459016, 2009.

Petit, J.-E., Favez, O., and Chauvigné, A.: Deliverable D5 (D1.5) NRT Source Apportionment Service Tools for submicron carbonaceous matter (final), Tech. rep., RI-URBANS Research Infrastructures Services Reinforcing Air Quality Monitoring Capacities in European Urban & Industrial AreaS (GA n. 101036245), https://riurbans.eu/wp-content/uploads/2024/12/RI-URBANS_D5_D1_5.pdf, 2024.

Pletscher, K., Weiß, M., and Mölter, L.: Simultaneous determination of PM fractions, particle number and particle size distribution in high time resolution applying one and the same optical measurement technique, Gefahrst. Reinhalt. L., 76, 425–436, 2016.

Regione Valle d'Aosta: Aerial photograph of Aosta from GeoBrowser, https://mappe.regione.vda.it/pub/geoCartoSCT/, 2021.

Rigler, M., Drinovec, L., Lavrič, G., Vlachou, A., Prévôt, A. S. H., Jaffrezo, J. L., Stavroulas, I., Sciare, J., Burger, J., Kranjc, I., Turšič, J., Hansen, A. D. A., and Močnik, G.: The new instrument using a TC–BC (total carbon–black carbon) method for the online measurement of carbonaceous aerosols, Atmos. Meas. Tech., 13, 4333–4351, https://doi.org/10.5194/amt-13-4333-2020, 2020.

Rivas, I., Beddows, D. C., Amato, F., Green, D. C., Järvi, L., Hueglin, C., Reche, C., Timonen, H., Fuller, G. W., Niemi, J. V., Pérez, N., Aurela, M., Hopke, P. K., Alastuey, A., Kulmala, M., Harrison, R. M., Querol, X., and Kelly, F. J.: Source apportionment of particle number size distribution in urban background and traffic stations in four European cities, Environ. Int., 135, 105 345, https://doi.org/10.1016/j.envint.2019.105345, 2020.

Rolph, G., Stein, A., and Stunder, B.: Real-time Environmental Applications and Display sYstem: READY, Environ. Modell. Softw., 95, 210–228, https://doi.org/10.1016/j.envsoft.2017.06.025, 2017.

Romonosky, D. E., Ali, N. N., Saiduddin, M. N., Wu, M., Lee, H. J. J., Aiona, P. K., and Nizkorodov, S. A.: Effective absorption cross sections and photolysis rates of anthropogenic and biogenic secondary organic aerosols, Atmos. Environ., 130, 172–179, https://doi.org/10.1016/j.atmosenv.2015.10.019, 2016.

Salma, I., Ocskay, R., Raes, N., and Maenhaut, W.: Fine structure of mass size distributions in an urban environment, Atmos. Environ., 39, 5363–5374, https://doi.org/10.1016/j.atmosenv.2005.05.021, 2005.

Savadkoohi, M., Pandolfi, M., Favez, O., Putaud, J.-P., Eleftheriadis, K., Fiebig, M., Hopke, P. K., Laj, P., Wiedensohler, A., Alados-Arboledas, L., Bastian, S., Chazeau, B., Álvaro Clemente María, Colombi, C., Costabile, F., Green, D. C., Hueglin, C., Liakakou, E., Luoma, K., Listrani, S., Mihalopoulos, N., Marchand, N., Monik, G., Niemi, J. V., Ondráek, J., Petit, J.-E., Rattigan, O. V., Reche, C., Timonen, H., Titos, G., Tremper, A. H., Vratolis, S., Vodika, P., Funes, E. Y., Zíková, N., Harrison, R. M., Petäjä, T., Alastuey, A., and Querol, X.: Recommendations for reporting equivalent black carbon (eBC) mass concentrations based on long-term pan-European in-situ observations, Environ. Int., 185, 108 553, https://doi.org/10.1016/j.envint.2024.108553, 2024.

Savadkoohi, M., Sofowote, U. M., Querol, X., Alastuey, A., Pandolfi, M., and Hopke, P. K.: Source-dependent absorption Ångström exponent in the Los Angeles Basin: Multi-time resolution factor analyses of ambient PM2.5 and aerosol optical absorption, Sci. Total Environ., 958, 178 095, https://doi.org/10.1016/j.scitotenv.2024.178095, 2025.

Sowlat, M. H., Hasheminassab, S., and Sioutas, C.: Source apportionment of ambient particle number concentrations in central Los Angeles using positive matrix factorization (PMF), Atmos. Chem. Phys., 16, 4849–4866, https://doi.org/10.5194/acp-16-4849-2016, 2016.

Stein, A. F., Draxler, R. R., Rolph, G. D., Stunder, B. J. B., Cohen, M. D., and Ngan, F.: NOAA's HYSPLIT Atmospheric Transport and Dispersion Modeling System, Bull. Amer. Meteor. Soc., 96, 2059 – 2077, https://doi.org/10.1175/BAMS-D-14-00110.1, 2015.

Thimmaiah, D., Hovorka, J., and Hopke, P. K.: Source apportionment of winter submicron prague aerosols from combined particle number size distribution and gaseous composition data, Aerosol Air Qual. Res., 9, 209–236, https://doi.org/10.4209/aaqr.2008.11.0055, 2009.

Vecchi, R., Bernardoni, V., Paganelli, C., and Valli, G.: A filter-based light-absorption measurement with polar photometer: Effects of sampling artefacts from organic carbon, J. Aerosol Sci., 70, 15–25, https://doi.org/10.1016/j.jaerosci.2013.12.012, 2014.

Vörösmarty, M., Hopke, P. K., and Salma, I.: Attribution of aerosol particle number size distributions to main sources using an 11-year urban dataset, Atmos. Chem. Phys., 24, 5695–5712, https://doi.org/10.5194/acp-24-5695-2024, 2024.

Vu, T. V., Delgado-Saborit, J. M., and Harrison, R. M.: Review: Particle number size distributions from seven major sources and implications for source apportionment studies, Atmos. Environ., 122, 114–132, https://doi.org/10.1016/j.atmosenv.2015.09.027, 2015.

Wang, Y., Hopke, P. K., Rattigan, O. V., Xia, X., Chalupa, D. C., and Utell, M. J.: Characterization of Residential Wood Combustion Particles Using the Two-Wavelength Aethalometer, Environ. Sci. Tech., 45, 7387–7393, https://doi.org/10.1021/es2013984, 2011.

Watson, J. G., Cooper, J. A., and Huntzicker, J. J.: The effective variance weighting for least squares calculations applied to the mass balance receptor model, Atmos. Environ. (1967), 18, 1347–1355, https://doi.org/10.1016/0004-6981(84)90043-X, 1984.

Weingartner, E., Saathoff, H., Schnaiter, M., Streit, N., Bitnar, B., and Baltensperger, U.: Absorption of light by soot particles: determination of the absorption coefficient by means of aethalometers, J. Aerosol Sci., 34, 1445–1463, https://doi.org/10.1016/S0021-8502(03)00359-8, 2003.

Wu, H., Li, Z., Jiang, M., Liang, C., Zhang, D., Wu, T., Wang, Y., and Cribb, M.: Contributions of traffic emissions and new particle formation to the ultrafine particle size distribution in the megacity of Beijing, Atmos. Environ., 262, 118 652, https://doi.org/10.1016/j.atmosenv.2021.118652, 2021.

Xie, M., Chen, X., Holder, A. L., Hays, M. D., Lewandowski, M., Offenberg, J. H., Kleindienst, T. E., Jaoui, M., and Hannigan, M. P.: Light absorption of organic carbon and its sources at a southeastern U.S. location in summer, Environ. Pollut., 244, 38–46, https://doi.org/10.1016/j.envpol.2018.09.125, 2019.

York, D., Evensen, N. M., Martínez, M. L., and De Basabe Delgado, J.: Unified equations for the slope, intercept, and standard errors of the best straight line, Am. J. Phys., 72, 367–375, https://doi.org/10.1119/1.1632486, 2004.

Zanatta, M., Gysel, M., Bukowiecki, N., Müller, T., Weingartner, E., Areskoug, H., Fiebig, M., Yttri, K., Mihalopoulos, N., Kouvarakis, G., Beddows, D., Harrison, R., Cavalli, F., Putaud, J., Spindler, G., Wiedensohler, A., Alastuey, A., Pandolfi, M., Sellegri, K., Swietlicki, E., Jaffrezo, J., Baltensperger, U., and Laj, P.: A European aerosol phenomenology-5: Climatology of black carbon optical properties at 9 regional background sites across Europe, Atmos. Environ., 145, 346–364, https://doi.org/10.1016/j.atmosenv.2016.09.035, 2016.

Zhou, L., Hopke, P. K., Paatero, P., Ondov, J. M., Pancras, J., Pekney, N. J., and Davidson, C. I.: Advanced factor analysis for multiple time resolution aerosol composition data, Atmos. Environ., 38, 4909–4920, https://doi.org/10.1016/j.atmosenv.2004.05.040, 2004.

Zhou, L., Hopke, P. K., Stanier, C. O., Pandis, S. N., Ondov, J. M., and Pancras, J. P.: Investigation of the relationship between chemical composition and size distribution of airborne particles by partial least squares and positive matrix factorization, J. Geophys. Res., 110, https://doi.org/10.1029/2004JD005050, 2005a.

Zhou, L., Kim, E., Hopke, P. K., Stanier, C., and Pandis, S. N.: Mining airborne particulate size distribution data by positive matrix factorization, J. Geophys. Res., 110, https://doi.org/10.1029/2004JD004707, 2005b.

Zotter, P., Herich, H., Gysel, M., El-Haddad, I., Zhang, Y., Močnik, G., Hüglin, C., Baltensperger, U., Szidat, S., and Prévôt, A. S. H.: Evaluation of the absorption Ångström exponents for traffic and wood burning in the Aethalometer-based source apportionment using radiocarbon measurements of ambient aerosol, Atmos. Chem. Phys., 17, 4229–4249, https://doi.org/10.5194/acp-17-4229-2017, 2017.